JGR Solid Earth

RESEARCH ARTICLE
10.1029/2018JB016920

Key Points:
- We developed a new method for direct inversion of 3-D Vs azimuthal anisotropy from surface wave traveltime data
- The new method considers period-dependent surface wave ray tracing based on 2-D isotropic phase velocity maps
- The obtained azimuthal anisotropy in Yunnan reveals apparent differences in upper crustal and upper mantle deformation styles

Supporting Information:
- Supporting Information S1

Correspondence to:
H. Yao and H.-Y. Yang,
hjyao@ustc.edu.cn;
hsinyingtw@gmail.com

Citation:
Liu, C., Yao, H., Yang, H.-Y., Shen, W., Fang, H., Hu, S., & Qiao, L. (2019). Direct inversion for three-dimensional shear wave speed azimuthal anisotropy based on surface wave ray tracing: Methodology and application to Yunnan, southwest China. *Journal of Geophysical Research: Solid Earth*, *124*, 11,394–11,413. https://doi.org/10.1029/2018JB016920

Received 29 OCT 2018
Accepted 20 AUG 2019
Accepted article online 23 AUG 2019
Published online 7 NOV 2019

Direct Inversion for Three-Dimensional Shear Wave Speed Azimuthal Anisotropy Based on Surface Wave Ray Tracing: Methodology and Application to Yunnan, Southwest China

Chuanming Liu[1,2], Huajian Yao[1,3], Hsin-Ying Yang[1,3], Weisen Shen[4], Hongjian Fang[1,5], Shaoqian Hu[1], and Lei Qiao[1]

[1]Laboratory of Seismology and Physics of Earth's Interior, School of Earth and Space Sciences, University of Science and Technology of China, Hefei, China, [2]Department of Physics, University of Colorado Boulder, Boulder, CO, USA, [3]CAS Center for Excellence in Comparative Planetology, Hefei, China, [4]Department of Geosciences, State University of New York at Stony Brook, Stony Brook, NY, USA, [5]Now at Department of Earth, Atmospheric and Planetary Sciences, Massachusetts Institute of Technology, Cambridge, MA, USA

Abstract Azimuthal anisotropy retrieved from surface waves is important for constraining depth-varying deformation patterns in the crust and upper mantle. We present a direct inversion technique for the three-dimensional shear wave speed azimuthal anisotropy based on mixed-path surface wave traveltime data. This new method includes two steps: (1) inversion for the 3-D isotropic *V*sv model directly from Rayleigh wave traveltimes and (2) joint inversion for both 3-D *V*sv azimuthal anisotropy and additional 3-D isotropic *V*sv perturbation. The joint inversion can significantly mitigate the trade-off between strong heterogeneity and anisotropy. With frequency-dependent ray tracing based on 2-D isotropic phase speed maps, the new method takes into account the ray-bending effect on surface wave propagation. We apply the new method to a regional array in Yunnan, southwestern China. Using Rayleigh wave phase velocity dispersion data in the period band of 5–40 s extracted from ambient noise interferometry, we obtain a 3-D model of shear wave speed and azimuthal anisotropy in the crust and uppermost mantle in Yunnan. This model reveals that two midcrust low-velocity zones are possible weak channels, and the azimuthal anisotropy at a depth of 5 to 30 km is mainly controlled by nearby strike-slip faults, some of which also approximately coincide with the lateral boundaries of the crustal low-velocity zones. Approximately south of 26°N, the upper crustal azimuthal anisotropy from our model is significantly different from the upper mantle anisotropy inferred by shear wave splitting, indicating different deformation styles between the crust and upper mantle in southern Yunnan.

1. Introduction

Seismic anisotropy is recognized as being indicative of the shape-preferred orientation of cracks or layered structures and the lattice-preferred orientation of mineral crystals under strain/stress (Crampin & Chastin, 2003; Savage, 1999). The seismic anisotropy retrieved from surface waves is a useful tool to investigate deformation fabrics and the history of tectonic evolution in the crust and uppermost mantle globally or regionally (Mainprice, 2007; Montagner, 1994; Savage, 1999; Yao et al., 2010). Surface waves have been widely used to invert for the radial and azimuthal anisotropy of shear wave velocity structures (e.g., Montagner & Tanimoto, 1991; Debayle et al., 2005; Marone & Romanowicz, 2007; Ekström, 2011; Zhu & Tromp, 2013; Xie et al., 2015). Radial anisotropy, referring to the wave speed differences between the vertical and lateral directions, is introduced to explain velocity discrepancies determined between Rayleigh and Love waves. Azimuthal anisotropy is invoked to resolve the wave speed variations of the Rayleigh waves propagating in different azimuthal directions. The development of ambient noise cross correlation allows us to obtain dispersive surface waves in the relatively short and intermediate period bands (e.g., Shapiro et al., 2004; Yao et al., 2006; Yang et al., 2007; Bense et al., 2007). Thus, the abundance of dispersion curves is capable of producing high-resolution shear wave images with the radial and azimuthal anisotropy in the crust and uppermost mantle over broad regions (e.g., Huang et al., 2010; Lin et al., 2010; Moschetti et al., 2010; Xie et al., 2013, 2017; Yao et al., 2010). In this study, we will focus on azimuthal anisotropy derived from surface waves.

In general, depth-dependent shear wave speed (*Vs*) azimuthal anisotropy can be obtained by pointwise inversion of the period-dependent Rayleigh wave dispersion data with azimuthal anisotropy. At first, period-dependent 2-D phase velocity maps with azimuthal anisotropy can be constructed by the tomographic inversion of mixed-path dispersion data (e.g., Barmin et al., 2001; Montagner, 1986; Yao et al., 2010) or from Eikonal tomography for short-period Rayleigh waves (Lin et al., 2009) and Helmholtz tomography (Lin & Ritzwoller, 2011) for long-period Rayleigh waves in regions with good azimuthal raypath coverage. With the approximately linear relationship between the elastic tensor coefficients and the effect of weak anisotropy on surface waves, Montagner and Nataf (1986) proposed a linearized inversion method to invert phase velocities for shear wave speed with azimuthal and radial anisotropy at depths. This method is widely applied to constrain azimuthal anisotropy in the upper mantle regionally (e.g., Montagner & Jobert, 1988; Silveira & Stutzmann, 2002; Yao et al., 2010; Yao, 2015) and globally (e.g., Montagner & Tanimoto, 1991). Based on Montagner and Nataf (1986), Xie et al. (2015, 2017) further inverted surface wave isotropic phase velocities and Rayleigh wave azimuthal anisotropy for the oriented elastic tensor of a titled anisotropic medium, considering radial and azimuthal anisotropy simultaneously. Aside from using phase velocity measurements extracted from waveforms, azimuthal anisotropy can also be retrieved from a two-step waveform inversion, which first inverts for 1-D path-averaged shear wave speed models from a nonlinear surface waveform inversion (Nolet, 1990), then obtains the 3-D shear velocity structures with azimuthal anisotropy by tomographic inversion (e.g., Debayle et al., 2005; Simons et al., 2002). Another way to obtain the depth-dependent azimuthal anisotropy is to perform the waveform inversion directly. Marone and Romanowicz (2007) developed a tomographic procedure to invert long-period surface waveforms for both the radial and azimuthal anisotropy, with shear wave splitting measurements as additional constraints. Using the spectral-element and adjoint methods, Zhu and Tromp (2013) obtained a 3-D azimuthally anisotropic model of Europe and the North Atlantic Ocean, which required a significant computational cost.

Fang et al. (2015) proposed a method that directly inverts all the path-dependent dispersion data for 3-D isotropic shear wave speed structures. In continuation of this work, we expand the method to further invert for azimuthal anisotropy in order to avoid the assumption of great-circle propagation commonly applied in most surface wave tomography studies. This method employs a frequency-dependent ray tracing of the surface waves using 2-D isotropic phase speed maps based on the fast marching method (Rawlinson & Sambridge, 2004). In section 2, we discuss the details of the method, and then in section 3, we perform synthetic tests to assess the reliability of this method. Finally, in sections 4 and 5, we apply this method to Yunnan in southwest China and discuss its tectonic implications.

2. Methodology

In this section, we describe the mathematical expression of the forward and inverse problems. Subsequently, we apply the proposed method to synthetic and real data to show the feasibility of direct inversion for azimuthal anisotropic structures.

2.1. The Forward Problem

As a consequence of structural heterogeneity, the raypath of Rayleigh waves may detour from the great-circle path between source and receiver. When we take the azimuthal anisotropy into account, the traveltime between Source A and Station B based on the ray theory is given by

$$t_{\mathrm{AB}}(\omega) = \int_{l_{\mathrm{AB}}} \frac{1}{c(l,\omega,\psi)}\mathrm{d}l, \tag{1}$$

where $c(l,\omega,\psi)$ is the local phase velocity along the actual raypath l_{AB}, ω is the angular frequency, and ψ is the azimuth of Rayleigh wave propagation (with respect to the north). Equation (1) can be discretized as

$$t_{\mathrm{AB}}(\omega) = \sum_{p=1}^{P} \frac{1}{c_p(\omega,\psi)}\Delta l, \tag{2}$$

where P means the number of path segments, p is the index of path segments, and $c_p(\omega,\psi)$ represents the phase velocity for the path segment Δl along AB. The Rayleigh wave phase velocity $c_p(\omega,\psi)$ has the following expression (Smith & Dahlen, 1973):

$$c_p(\omega,\psi) = c_0(\omega,p) + a_1(\omega,p)\cos 2\psi + a_2(\omega,p)\sin 2\psi + a_3(\omega,p)\cos 4\psi + a_4(\omega,p)\sin 4\psi, \tag{3}$$

where $c_0(\omega)$ is the isotropic phase speed and $a_{1,2}$ and $a_{3,4}$ are the amplitudes of 2ψ (180° periodicity) and 4ψ (90° periodicity) terms, respectively. As stated in Montagner and Nataf (1986), the 4ψ terms in equation (3) are negligible for Rayleigh waves.

We parameterize the study area for the forward problem on a 2-D spherical surface with a regular grid of K points in total. The 1-D transversely isotropic layered model Θ_k at each grid point k is taken as a reference with the isotropic phase speed given by c_0^k. The 2-D phase velocity map at frequency ω can be estimated by $\widehat{c}_k(\omega,\psi)$ $\left(\widehat{c}_k(\omega,\psi) = c_0^k(\omega) + a_1^k(\omega)\cos 2\psi + a_2^k(\omega)\sin 2\psi, k = 1,2,...K\right)$. We use bilinear interpolation to calculate the phase velocity along a path segment p:

$$\frac{1}{c_p(\omega,\psi)} = \sum_{k=1}^{K} \frac{\nu_{pk}}{c_0^k(\omega) + a_1^k(\omega)\cos 2\psi + a_2^k(\omega)\sin 2\psi}, \tag{4}$$

where ν_{pk} is the bilinear interpolation coefficient, describing the weight of each grid point k for a specific path segment p. The phase velocity at the kth grid point, $\widehat{c}_k(\omega,\psi)$, can be obtained from the 1-D transversely isotropic layered model Θ_k:

$$\widehat{c}_k(\omega,\psi) = g(\Theta_k,\omega,\psi), \tag{5}$$

where $g(\Theta_k,\omega,\psi)$ is a forward function that maps Θ_k to the frequency-dependent phase/group velocities, which can be calculated by using the transfer matrix method for layered media with a half-space (Haskell, 1953; Herrmann, 2013; Thomson, 1950) or the normal-mode method for spherical media (e.g., Dahlen & Tromp, 1998; Woodhouse, 1988; Yang et al., 2010).

The ith Rayleigh wave traveltime measurement at frequency ω is given by

$$\begin{aligned} t_i(\omega) &= \sum_{p=1}^{P} \frac{1}{c_{ip}(\omega,\psi)}\Delta l_i = \sum_{p=1}^{P}\sum_{k=1}^{K} \frac{\nu_{pk}^i}{c_0^k(\omega) + a_1^k(\omega)\cos 2\psi + a_2^k(\omega)\sin 2\psi}\Delta l_i \\ &= \sum_{k=1}^{K} \frac{\mu_{ik}}{c_0^k(\omega) + a_1^k(\omega)\cos 2\psi + a_2^k(\omega)\sin 2\psi}, \end{aligned} \tag{6}$$

where $\mu_{ik} = \sum_{p=1}^{P} \nu_{pk}^i \Delta l_i$ and ν_{pk}^i are the bilinear interpolation coefficients along the raypath for the ith traveltime data point. Here we assume the azimuthally anisotropic phase velocity variations are typically several percent in magnitude, which are much smaller than the isotropic phase velocity variations. Therefore, the raypath at each frequency ω is computed by the fast-marching method (Rawlinson & Sambridge, 2004) based only on the 2-D isotropic part phase velocities $c_0^k(\omega)$.

2.2. The Inverse Problem

We intend to recover a tomographic model that can be obtained by minimizing the traveltime difference between the observed traveltimes $t_i^{\mathrm{obs}}(\omega)$ and the model predictions for all frequencies ω. If we take the perturbation of the traveltime t_i in equation (6) and use the isotropic phase speed $c_0^k(\omega)$ as a reference, the traveltime difference between the measurement $t_i^{\mathrm{obs}}(\omega)$ and the reference isotropic model prediction $t_i^{\mathrm{ref}}(\omega)$ can be approximated by

$$\begin{aligned} \delta t_i(\omega) &= t_i^{\mathrm{obs}}(\omega) - t_i^{\mathrm{ref}}(\omega) \approx \sum_{k=1}^{K} \frac{-\mu_{ik}}{\left(c_0^k(\omega)\right)^2}\left(\delta c_k(\omega) + a_1^k(\omega)\cos 2\psi + a_2^k(\omega)\sin 2\psi\right) \\ &= \sum_{k=1}^{K} \frac{-\mu_{ik}}{\left(c_0^k(\omega)\right)^2}\left(\delta c_k^{\mathrm{ETI}}(\omega) + \delta c_k^{\mathrm{AA}}(\omega,\psi)\right). \end{aligned} \tag{7}$$

Note that the phase velocity perturbation is further decomposed into $\delta c_k^{\mathrm{ETI}}(\omega) = \delta c_k(\omega)$ and $\delta c_k^{\mathrm{AA}}(\omega,\psi) = a_1^k(\omega)\cos 2\psi + a_2^k(\omega)\sin 2\psi$ (Montagner & Nataf, 1986) due to the variations in effective transversely isotropic moduli (ETI) and azimuthally anisotropic moduli (AA) relative to the reference moduli, respectively.

From Fang et al. (2015) and Yao (2015), the isotropic perturbation in Rayleigh wave phase velocity with respect to the isotropic reference model can be expressed as

$$\delta c_k^{\mathrm{ETI}}(\omega) = \int_0^{\infty} \left(\frac{\partial c_k(\omega)}{\partial \alpha_k(z)} \delta\alpha_k(z) + \frac{\partial c_k(\omega)}{\partial \beta_k(z)} \delta\beta_k(z) + \frac{\partial c_k(\omega)}{\partial \rho_k(z)} \delta\rho_k(z) \right) \mathrm{d}z, \tag{8}$$

where α, β, and ρ are the compressional wave speed (V_{PH}) of horizontally propagating P waves, shear wave speed (V_{SV}) of vertically polarized S waves propagating horizontally, and mass density, respectively. By using an empirical relationship (Brocher, 2005), we can relate compressional wave speed and density to shear wave speed. Then $\delta\alpha(z) = R_\alpha(z)\delta\beta(z)$ and $\delta\rho(z) = R_\rho(z)\delta\beta(z)$, where $R_\alpha(z)$ and $R_\rho(z)$ are corresponding empirical relationship functions (Fang et al., 2015). By discretizting the integral in equation (8) in terms of the depth nodes z_j, we can get

$$\delta c_k^{\mathrm{ETI}}(\omega) = \sum_{j=1}^{J} \left[\left(\int_{z_j}^{z_{j+1}} \frac{\partial c_k(\omega)}{\partial \alpha_k(z)} \, \mathrm{d}z \right) R_\alpha(z_j) + \left(\int_{z_j}^{z_{j+1}} \frac{\partial c_k(\omega)}{\partial \beta_k(z)} \, \mathrm{d}z \right) + \left(\int_{z_j}^{z_{j+1}} \frac{\partial c_k(\omega)}{\partial \rho_k(z)} \, \mathrm{d}z \right) R_\rho(z_j) \right] \delta\beta_k(z_j). \tag{9}$$

Here, J is the number of layers at depth and j is the index of the depth nodes.

In addition, according to Montagner and Nataf (1986), the effective transversely isotropic perturbation can also be represented as

$$\delta c_k^{\mathrm{ETI}}(\omega) = \int_0^{\infty} \left(\frac{\partial c_k(\omega)}{\partial A_k(z)} \delta A_k(z) + \frac{\partial c_k(\omega)}{\partial C_k(z)} \delta C_k(z) + \frac{\partial c_k(\omega)}{\partial L_k(z)} \delta L_k(z) + \frac{\partial c_k(\omega)}{\partial F_k(z)} \delta F_k(z) \right) dz, \tag{10}$$

where the four parameters (A, C, L, and F) in equation (10) together with another N, represent the transversely isotropic medium with $A = \rho V_{\mathrm{PH}}^2, C = \rho V_{\mathrm{PV}}^2, L = \rho V_{\mathrm{SV}}^2, N = \rho V_{\mathrm{SH}}^2$, and $F = \eta(A - 2L)$. Here, ρ is the density, V_{PH} and V_{PV} are the velocities of horizontally and vertically propagating P waves, and V_{SH} and V_{SV} are the velocities of horizontally and vertically polarized S waves propagating horizontally. Since we do not include Love wave data and assume $V_{\mathrm{PH}} = V_{\mathrm{PV}}, V_{\mathrm{SH}} = V_{\mathrm{SV}}, \eta = 1$, the difference between equations (8) and (10) is very small in this case. So we use equations (8) and (9) to represent the isotropic phase velocity perturbation for the later inversion scheme for isotropic shear velocities.

According to Montagner and Nataf (1986), the azimuthally anisotropic perturbation to the phase velocity of Rayleigh waves can be written as

$$\begin{aligned} \delta c_k^{\mathrm{AA}}(\omega, \psi) = \int_0^{\infty} \Bigg[& \left(B_c^k \frac{\partial c_k(\omega)}{\partial A_k} + G_c^k \frac{\partial c_k(\omega)}{\partial L_k} + H_c^k \frac{\partial c_k(\omega)}{\partial F_k} \right) \cos 2\psi \\ & + \left(B_s^k \frac{\partial c_k(\omega)}{\partial A_k} + G_s^k \frac{\partial c_k(\omega)}{\partial L_k} + H_s^k \frac{\partial c_k(\omega)}{\partial F_k} \right) \sin 2\psi \Bigg] \, \mathrm{d}z, \end{aligned} \tag{11}$$

where B_c, B_s, G_c, G_s, H_c, and H_s represent the 2ψ azimuthal variations of A, L, and F, respectively. Since the $\frac{\partial c}{\partial F}$ is much smaller than $\frac{\partial c}{\partial L}$ (Montagner & Nataf, 1986; Xie et al., 2015), the effect of $H_{c,s}$ on the Rayleigh wave phase velocities is neglected such that we can approximate the azimuthally anisotropic perturbation in the Rayleigh wave phase velocities by

$$\delta c_k^{\mathrm{AA}}(\omega, \psi) \approx \int_0^{\infty} \left[\left(B_c^k \frac{\partial c_k(\omega)}{\partial A_k} + G_c^k \frac{\partial c_k(\omega)}{\partial L_k} \right) \cos 2\psi + \left(B_s^k \frac{\partial c_k(\omega)}{\partial A_k} + G_s^k \frac{\partial c_k(\omega)}{\partial L_k} \right) \sin 2\psi \right] \mathrm{d}z \tag{12}$$

The Rayleigh wave phase velocity is mainly sensitive to L and the shallow crustal A (e.g., Xie et al., 2015), which makes it challenging to retrieve exact values for $G_{c,s}$ and $B_{c,s}$ simultaneously. In view of studies of mica-rich and amphibole-rich crustal rocks (Barruol & Kern, 1996) as well as olivine-dominated mantle rocks (Montagner & Nataf, 1986), it is appropriate to assume $\frac{B_{c,s}}{A} = \frac{G_{c,s}}{L}$ (Lin et al., 2010; Yao, 2015). The simplification will lead to the identical direction of fast axes in V_{PH} and V_{SV} and influence the amplitude of the absolute azimuthal anisotropy. By discretization of the integral in equation (12) in terms of the depth node z_j and the assumption of $\frac{\mathrm{B}_{c,s}^{j}}{A_j} = \frac{G_{c,s}^{j}}{L_j}$ for each depth interval $[z_j, z_{j+1}]$, we can obtain equation (13)

$$\delta c_k^{\mathrm{AA}}(\omega,\psi)\approx\sum_{j=1}^{J}\left[\left(\int_{z_j}^{z_{j+1}}\frac{\partial c_k(\omega)}{\partial A_k(z)}\,\mathrm{d}z\right)A_k(z_j)+\left(\int_{z_j}^{z_{j+1}}\frac{\partial c_k(\omega)}{\partial L_k(z)}\,\mathrm{d}z\right)L_k(z_j)\right]\left(\cos 2\psi\frac{G_c^k(z_j)}{L_k(z_j)}+\sin 2\psi\frac{G_s^k(z_j)}{L_k(z_j)}\right). \quad (13)$$

Finally, after inserting equations (9) and (13) into equation (7), we obtain

$$\begin{aligned}\delta t_i(\omega)=\sum_{k=1}^{K}\frac{-1}{\left(c_0^k(\omega)\right)^2}\sum_{j=1}^{J}\Bigg\{&\mu_{ik}\left[\left(\int_{z_j}^{z_{j+1}}\frac{\partial c_k(\omega)}{\partial\alpha_k(z)}\,\mathrm{d}z\right)R_\alpha(z_j)+\left(\int_{z_j}^{z_{j+1}}\frac{\partial c_k(\omega)}{\partial\beta_k(z)}\,\mathrm{d}z\right)\right.\\&\left.+\left(\int_{z_j}^{z_{j+1}}\frac{\partial c_k(\omega)}{\partial\rho_k(z)}\,dz\right)R_\rho(z_j)\right]\delta\beta_k(z_j)+\eta_{ik}\left[\left(\int_{z_j}^{z_{j+1}}\frac{\partial c_k(\omega)}{\partial A_k(z)}\,\mathrm{d}z\right)A_k(z_j)\right.\\&\left.+\left(\int_{z_j}^{z_{j+1}}\frac{\partial c_k(\omega)}{\partial L_k(z)}\,\mathrm{d}z\right)L_k(z_j)\right]\frac{G_c^k(z_j)}{L_k(z_j)}+\xi_{ik}\left[\left(\int_{z_j}^{z_{j+1}}\frac{\partial c_k(\omega)}{\partial A_k(z)}\,dz\right)A_k(z_j)\right.\\&\left.+\left(\int_{z_j}^{z_{j+1}}\frac{\partial c_k(\omega)}{\partial L_k(z)}\,\mathrm{d}z\right)L_k(z_j)\right]\frac{G_s^k(z_j)}{L_k(z_j)}\Bigg\},\end{aligned} \quad (14)$$

where $\eta_{ik}=\sum_{p=1}^{P}v_{pk}^i\cos 2\psi_p^i\Delta l_i$, and $\xi_{ik}=\sum_{p=1}^{P}v_{pk}^i\sin 2\psi_p^i\Delta l_i$. Here, i is the index of the Rayleigh wave traveltime measurements, j is the index of depth nodes, k indicates the index of horizontal grid points, and v_{pk}^i is the bilinear interpolation coefficient for the ith traveltime data point. Equation (14) can be represented in the form

$$\mathbf{d}=\mathbf{G}\mathbf{m}, \quad (15)$$

where $\mathbf{d}$ is the vector of the Rayleigh wave traveltime residuals for all frequencies and all paths, $\mathbf{G}$ is the data sensitivity matrix, and the model parameter vector $\mathbf{m}$ is given by

$$\mathbf{m}=\left[\delta\beta_1(z_1)\ldots\delta\beta_1(z_J)\ldots\delta\beta_K(z_J)\ \frac{G_c^1(z_1)}{L_1(z_1)}\ldots\frac{G_c^1(z_J)}{L_1(z_J)}\ldots\frac{G_c^K(z_J)}{L_K(z_J)}\ \frac{G_s^1(z_1)}{L_1(z_1)}\ldots\frac{G_s^1(z_J)}{L_1(z_J)}\ldots\frac{G_s^K(z_J)}{L_K(z_J)}\right]^T. \quad (16)$$

Equation (15) can be solved by the LSQR algorithm (Paige & Saunders, 1982) with the regularized inversion system:

$$\begin{bmatrix}\mathbf{G}_{\mathrm{iso}} & \mathbf{G}_{\mathrm{AA}}\\ \lambda_1\mathbf{L}_{\mathrm{iso}} & \mathbf{0}\\ \mathbf{0} & \lambda_2\mathbf{L}_{\mathrm{AA}}\end{bmatrix}\begin{bmatrix}\mathbf{m}_{\mathrm{iso}}\\ \mathbf{m}_{\mathrm{AA}}\end{bmatrix}=\begin{bmatrix}\mathbf{d}\\ \mathbf{0}\\ \mathbf{0}\end{bmatrix}, \quad (17)$$

where $\mathbf{G}_{\mathrm{iso}}$ and $\mathbf{m}_{\mathrm{iso}}$ correspond to the first part of equation (14) about the isotropic perturbation to Vsv (i.e., $\delta\beta_k(z_j)$), $\mathbf{G}_{\mathrm{AA}}$ and $\mathbf{m}_{\mathrm{AA}}$ correspond to the second part of equation (14) about the azimuthally anisotropic perturbation (i.e., $\frac{G_c^k(z_j)}{L_k(z_j)}$ and $\frac{G_s^k(z_j)}{L_k(z_j)}$), $\mathbf{L}_{\mathrm{iso}}$ and $\mathbf{L}_{\mathrm{AA}}$ are the roughening matrices, and λ_1 and λ_2 are weighting parameters balancing data fitting and model regularization. $\mathbf{L}_{\mathrm{iso}}$ and $\mathbf{L}_{\mathrm{AA}}$ are usually represented by a finite-difference operator for Tikhonov regularization, which can be chosen as the first- or second-order spatial derivative operator (Aster et al., 2013) or a Gaussian spatial smoothing operator (Liu & Yao, 2016). In each iteration of inversion, since the isotropic Vsv model has been updated iteratively, new raypaths and new depth-dependent sensitivity kernel matrices ($\mathbf{G}_{\mathrm{iso}}$ and $\mathbf{G}_{\mathrm{AA}}$) for all isotropic and anisotropic parameters are updated as well.

To give a better view of our method, we divide the whole workflow into three steps: (1) preparation of period-dependent interstation Rayleigh wave phase velocity dispersion and traveltime data, which can be achieved from either ambient noise cross-correlations or earthquake data; (2) inversion for an isotropic Vsv model using a 3-D direct isotropic inversion method (DSurfTomo; Fang et al., 2015); and (3) taking the isotropic Vsv model from step (2) as the 3-D isotropic reference model to perform the 3-D joint inversion iteratively for both additional 3-D isotropic Vsv perturbation and azimuthal anisotropy. Although we include the isotropic Vsv perturbation in the joint inversion in Step (3), Step (2) is still necessary since it can provide a more reliable initial isotropic model, accelerating the convergence of the inversion. We refer to our whole two-step

inversion workflow as direct inversion for 3-D azimuthally anisotropic shear velocities from surface (Rayleigh) wave traveltimes (abbreviated as DAzimSurfTomo).

Finally, the azimuthally anisotropic velocity of the vertically polarized S waves propagating horizontally is given by

$$\widehat{V}_{\mathrm{SV}} \approx \sqrt{\frac{L + G_c \cos 2\psi + G_s \sin 2\psi}{\rho}}. \tag{18}$$

As G_c and G_s are usually much smaller than L, equation (18) can be approximated as

$$\widehat{V}_{\mathrm{SV}} \approx V_{\mathrm{SV}} \left(1 + \frac{G_c}{2L}\cos 2\psi + \frac{G_s}{2L}\sin 2\psi\right) = V_{\mathrm{SV}}[1 + A_{\mathrm{SV}}\cos 2(\psi - \phi)], \tag{19}$$

where V_{SV} is the isotropic part of vertically polarized S wave velocity and A_{SV} and ϕ are the anisotropy amplitude and the azimuth of fast polarization axis, respectively, which can be written as

$$A_{\mathrm{SV}} = \frac{1}{2}\sqrt{\left(\frac{G_s}{L}\right)^2 + \left(\frac{G_c}{L}\right)^2}, \tag{20}$$

$$\phi = \frac{1}{2}\tan^{-1}\left(\frac{G_s}{G_c}\right). \tag{21}$$

According to the error transfer formula (Yuan & Beghein, 2018), we can evaluate the robustness of the inversion results by giving the uncertainties of the magnitude A_{SV} and the azimuth of fast axis ϕ, respectively, as

$$\sigma^2_{A_{\mathrm{SV}}} = \frac{G_s^2\sigma^2_{G_s} + G_c^2\sigma^2_{G_c}}{4L^2(G_s^2 + G_c^2)}, \tag{22}$$

$$\sigma^2_{\phi} = \frac{1}{4}\frac{G_c^2\sigma^2_{G_s} + G_s^2\sigma^2_{G_c}}{(G_s^2 + G_c^2)^2}, \tag{23}$$

where the variances $\sigma^2_{G_c}$ and $\sigma^2_{G_s}$ are the diagonals of the model covariance matrix Cov($\mathbf{m}$) for the least squares solution; that is,

$$\mathrm{Cov}(\mathbf{m}) = \left(\mathbf{G}_w^T\mathbf{G}_w\right)^{-1}\mathbf{G}_w^T\mathrm{Cov}(\mathbf{d}_w)\mathbf{G}_w\left(\mathbf{G}_w^T\mathbf{G}_w\right)^{-1}, \tag{24}$$

where $\mathbf{W}$ is a diagonal matrix of data weighting, $\mathbf{G}_w = \mathbf{WG}$, $\mathbf{d}_w = \mathbf{Wd}$, and Cov($\mathbf{d}_w$) is the weighted data covariance matrix.

In addition, we can also estimate the uncertainties by applying the Monte Carlo error propagation technique (Aster et al., 2013; Fang et al., 2015), in which we simulate a collection of noisy data sets and then calculate the standard deviation of the ensemble of obtained models.

3. Synthetic Tests and Methodology Evaluation

In this section, we show how to obtain shear wave speed azimuthal anisotropy from the Rayleigh wave dispersion measurements through the proposed DAzimSurfTomo method above and evaluate the robustness and reliability of inversion results through different synthetic tests. First, we apply direct inversion of the Rayleigh wave dispersion data to generate 3-D isotropic Vsv structure (Fang et al., 2015), and then we use this inversion result as the reference model to invert for the 3-D shear wave speed azimuthal anisotropy.

3.1. Performance of the Proposed Method

To investigate the performance of our method, we carry out synthetic experiments with a 3-D anisotropic model. Figure 1 shows the virtual station distribution used in the synthetic test as well as the density of the raypath coverage. The average station spacing is about 30 km. The number of raypaths that connect

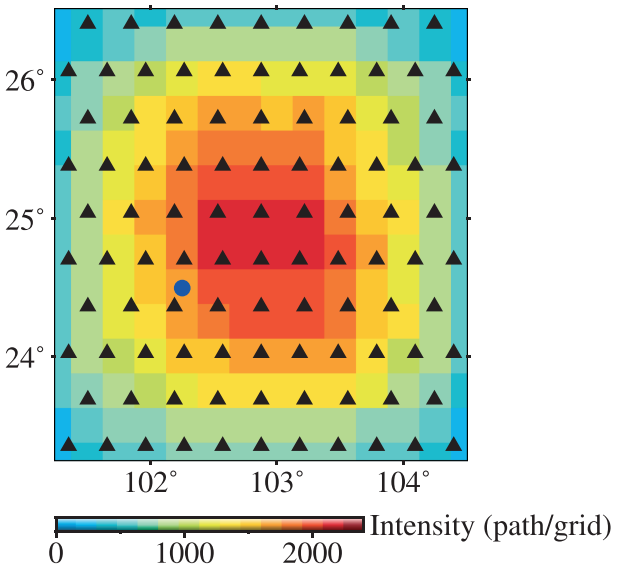

Figure 1. The station configuration used in the synthetic tests. The station locations are shown as black triangles. The blue dot indicates the location of a grid point (102.25°, 24.5°) used in Figure 5. The background color represents the density of the raypath coverage.

every two stations is 4,950 for every period. The period band of the synthetic Rayleigh wave dispersion measurements is set to range from 5 to 40 s, similar to the period range of the real ambient noise data we used in Yunnan, southwest China. Figure 2 shows an example of the depth sensitivity kernels for Rayleigh wave phase velocity with respect to perturbations in L and A at periods of 10 and 30 s. It is obvious that Rayleigh waves are sensitive to the deeper structure of L than of A for the same period and the longer period waves have a more pronounced sensitivity to the deeper structure. The isotropic Vsv model is composed of checkerboard-like velocity anomalies decaying laterally in the form of Gaussian functions for the seven layers (0–5, 5–10, 10–16, 16–24, 24–32, 32–42, and 42–54 km). The peak perturbations of the high- and low-velocity anomalies are ±10%, respectively. The relative magnitudes of the azimuthal anisotropy are set to be 2%, 4%, and 6% for the top two, the intermediate two, and the bottom three layers, respectively. Their corresponding fast polarization directions are shown in Figure 3, where the fast directions in different blocks at the same depth are perpendicular to each other. The study region is parameterized with 16 by 16 grid points with a grid interval of 0.25° in both latitude and longitude.

The synthetic interstation Rayleigh wave traveltimes are divided into two parts: the traveltime caused by the isotropic model (computed by the fast-marching method) and the traveltime produced by the azimuthally anisotropic model (using the same raypaths as those in the isotropic model). This means that we ignore the effect of the weak azimuthal anisotropy on the raypaths. To test the feasibility of our approach, we first consider synthetic traveltime data without noise and invert the data using the process described above. The influence of noise level will be discussed later in this section. In the first step, we use a uniform isotropic Vsv model as an initial model to perform the first step of direct inversion for the 3-D isotropic shear wave speed structure. Since we do not invert for radial anisotropy, we assume $V_{SH} = V_{SV}$ and

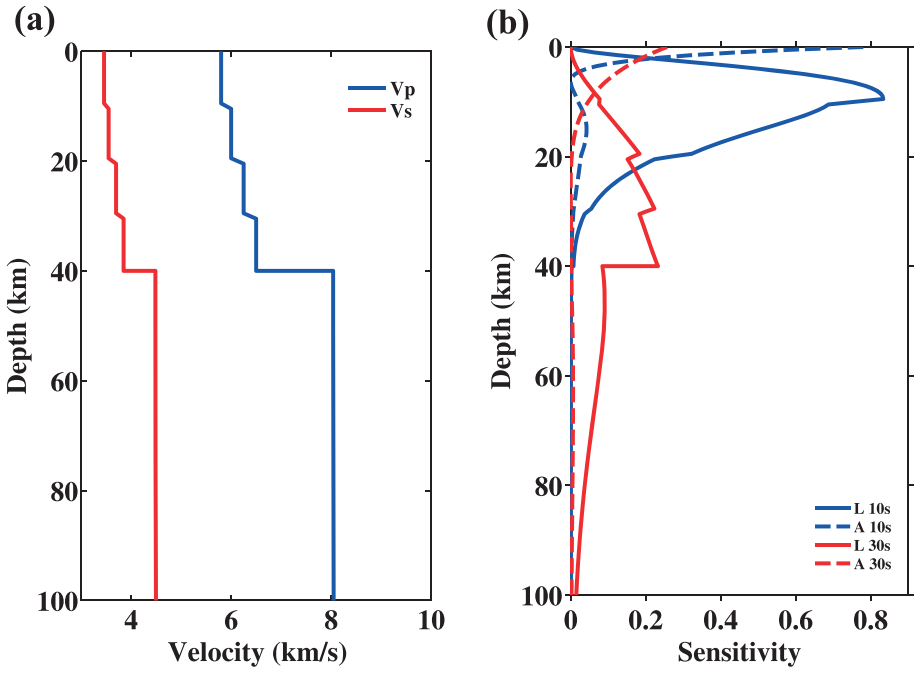

Figure 2. The 1-D velocity model (a) and its corresponding depth sensitivity kernels (b) for Rayleigh wave phase speeds at 10 and 30 s with respect to perturbations in L and A as a function of depth.

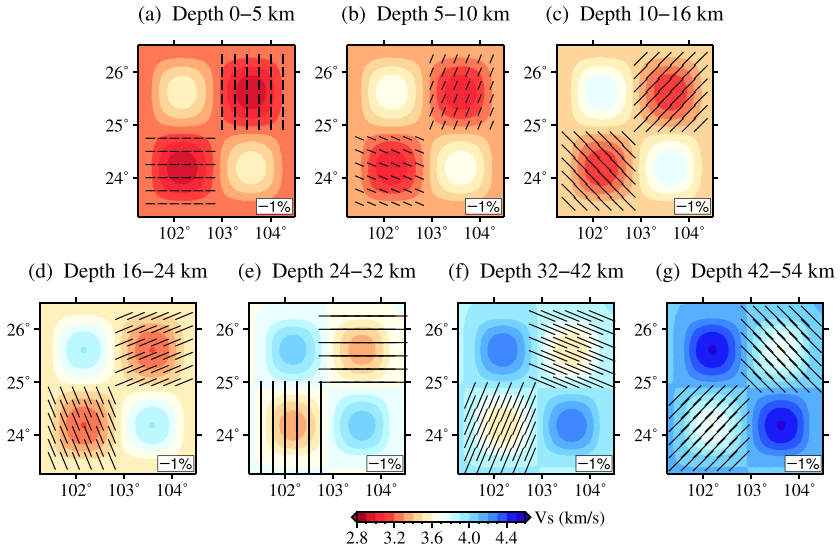

Figure 3. (a-g) Lateral slices of the input model in seven layers. *Vs* is color coded from blue (fast) to red (slow). The black bars show the magnitude (in percent) and the fast polarization direction of the azimuthal anisotropy

$V_{PH} = V_{PV}$. Based on the isotropic *V*sv result together with empirical relationships between the compressional wave speed, density, and shear wave speed (Brocher, 2005), we construct an initial isotropic model and calculate the corresponding sensitivity kernels of $\frac{\partial c}{\partial L}$ and $\frac{\partial c}{\partial A}$. Finally, we minimize the traveltime residuals between the measurements and predictions to invert for the 3-D isotropic *V*sv perturbation and azimuthally anisotropic structure (see equations (14) and (17)).

The resulting images (Figure 4) suggest that the isotropic *V*sv structure can be resolved very well in whole regions, and the azimuthally anisotropic pattern can be well retrieved to some extent in areas with good ray-path coverage. The angle differences between the inversion results and the input are listed in Table S1 in the supporting information, indicating that the average angle difference is approximately 5.4°. The angle difference of the first layer is the largest, which can be attributed to the fact that the shortest period data used in the synthetic test (5 s) cannot provide sufficient constraints on the shallowest structure. We also calculate azimuthally anisotropic phase velocity maps at different periods (10, 20, and 30 s; Figures S1a–S1f) from the 3-D azimuthally anisotropic shear velocity model and pick up one grid point (102.25°, 24.5°) to compare the predicted dispersion data with the input (Figure 5a). The comparison shows the fitting of the isotropic phase speed dispersion and the corresponding azimuthal anisotropy is excellent. After 3-D joint inversion, the standard deviation of the traveltime residuals is reduced from 172 ms (for 3-D isotropic starting model) to 102 ms (Figure 6a).

3.2. The Effect of Noise Level of the Synthetic Data

The noise level of the synthetic data will affect the recovery of the isotropic speed model in the first step, the isotropic inversion, and therefore influence the next step, joint inversion, as well as traveltime data fitting. We add 1% random Gaussian noise, which is the general uncertainty level of Rayleigh wave phase velocity measurements, to the synthetic traveltime data and then invert for the 3-D azimuthal anisotropy following our two-step 3-D anisotropic inversion method. The results (Figure S2 and Table S1) suggest that with the noise level rising from 0% to 1%, the average angle deviation of the fast axes increases from 5.4° to 7.4°, especially for the first layer where the data constraint is relatively poor. Other than the fast axes, the recovery in the magnitudes of the phase velocity azimuthal anisotropy (Figure 5) gets worse when the data noise level increases. In addition, the discrepancies in the isotropic phase speed fitting are significant at shorter periods (5–10 s). The reason is that with the increase of the noise level in the traveltime data, the uncertainty of the isotropic inversion results will increase, such that the noise level of the computed traveltimes used in the subsequent joint inversion will be enlarged. A series of synthetic tests show that when the noise level increases, the azimuthal anisotropy pattern can still be retrieved although with increasing angle

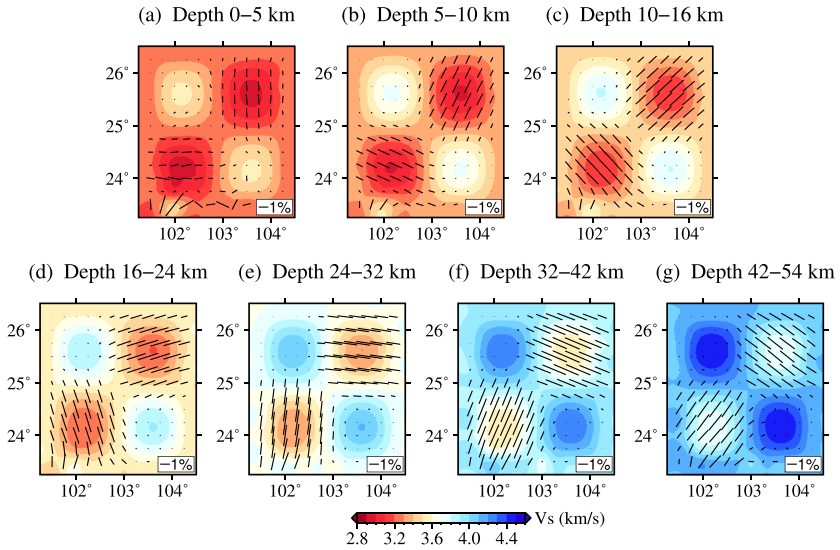

Figure 4. (a–g) The recovery of the input model in Figure 3 using synthetic data without noise.

deviations and reduced strength of anisotropy in the anisotropic model (Figures 5, S1, and S2 and Table S1) and increasing standard deviation of traveltime residuals (Figures 6a and 6b).

3.3. The Influence of the Assumption of Great-Circle-Path Propagation

Our method considers the frequency-dependent ray-bending effect with the fast-marching method (Rawlinson & Sambridge, 2004) in calculation of frequency-dependent traveltimes of Rayleigh waves in the first step of isotropic inversion (e.g., Fang et al., 2015; Li et al., 2016) and the second step of joint inversion, where we ignore the effect of the weak azimuthal anisotropy on the raypaths. Superior to the linearized ray theory that assumes the great-circle trajectory as in a homogeneous background medium, the generalized ray theory, which accounts for the ray-bending effect, is valid for strongly heterogeneous media (e.g., Yang & Hung, 2005). However, most studies of ambient noise surface wave tomography are based on linearized ray theory. To evaluate the importance of ray bending in tomography, we conduct a synthetic experiment under the great-circle-path assumption for comparison. The results from the great-circle-path propagation show large deviations in the anisotropic fast axes (Table S1 and Figure S3) and, accordingly, relatively bad fitting in the phase velocity azimuthal anisotropy (Figures 5 and S1). In addition, ignoring the ray-bending effect may increase the standard deviation of the traveltime residuals from 0.1 to 0.3 s.

3.4. Effects of the Trade-Off Between Heterogeneity and Anisotropy

To test the effects of the trade-off between heterogeneity and azimuthal anisotropy on our method with a dramatic change of isotropic and anisotropic patterns, we perform another synthetic test with a three-layer

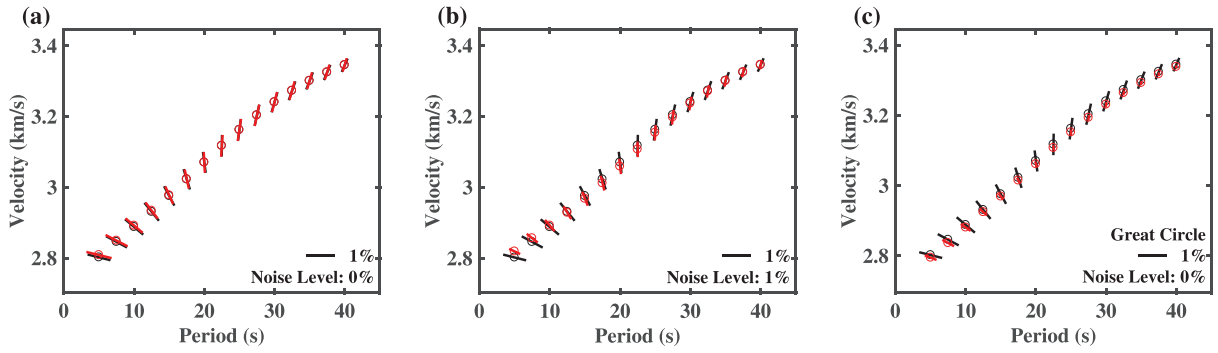

Figure 5. The comparison between the predicted (in red) and the input (in black) isotropic phase speed (circle) and its azimuthal anisotropy (bar) using data without noise (a), data with 1% Gaussian random noise (b), and noise-free data but under the assumption of great-circle-path propagation (c). Bars in the vertical direction indicate the N-S fast polarization axis, and the horizontal direction for the E-W fast axis.

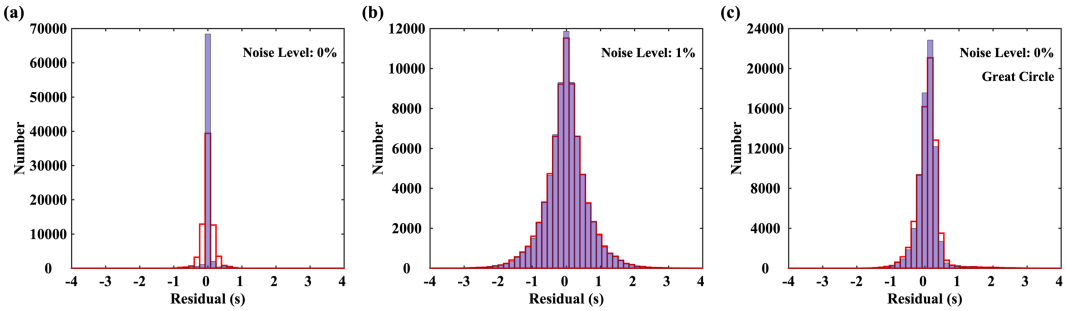

Figure 6. Distributions of Rayleigh wave traveltime residuals before (red) and after inversion (light blue) for three different cases: (a) input data without noise, (b) input data with 1% Gaussian random noise, and (c) input data without noise under the assumption of great-circle-path propagation.

model containing interdistributing high- and low-velocity bands with fast axes parallel or orthogonal to the bands, respectively. The peak perturbations of the high- and low-velocity anomalies are ±9% for each layer, respectively (Figures S4a–S4c). We use the same period range as the first synthetic test but add 20 more virtual stations to increase azimuthal coverage. Following the workflow of our two-step 3-D anisotropic inversion, the recovery of isotropic velocity is excellent (Figures S4d–S4f). The input amplitude of anisotropy is 1.5%, 2.5%, and 3% for the three layers, respectively. The recovery of the amplitude of azimuthal anisotropy in Layer 1 is worse than that of the other two layers due to the limitation of periods (5–40 s). The amplitude in the third layer is a bit overestimated. The joint inversion can retrieve about 73% of the amplitude of the input azimuthal anisotropy for the top two layers. The general pattern of azimuthal anisotropy, both in amplitudes and fast directions, can be retrieved properly, except for the transitional area (Figures S4d–S4f). The trade-off between the strong heterogeneity and anisotropy in this area tends to cause the fast direction to deviate from the input and result in reduced strength of azimuthal anisotropy. We have also tested the inversion of azimuthal anisotropy alone in the second step inversion, which gives a generally similar pattern to the joint inversion, but our joint inversion strategy can improve the recovery, especially in areas with a strong trade-off between heterogeneity and anisotropy. The joint inversion approach also appears to be more resistant to the data noise level.

4. Application to Yunnan, Southwest China

We applied our direct inversion method to Yunnan, southwest China, which is at the southeastern margin of the Tibetan Plateau. The collision between the Indian and Eurasian plates has caused the evolution of Tibetan Plateau over the past approximately 50 Myr (Molnar & Tapponnier, 1975; Royden et al., 2008), leaving a series of problems under debate, among which the key question is how the plateau and surrounding regions have deformed in response to the plate convergence. Serval models have been proposed to answer this question, including the rigid block extrusion model (Tapponnier et al., 1982, 2001), the continuous deformation model (Houseman & England, 1993; Molnar & Tapponnier, 1975), and the crustal channel flow model (Royden, 1997; Royden et al., 2008). Another controversy includes the mechanical coupling or decoupling between the crust and upper mantle, which is also related to the mechanism of plateau deformation. Some studies argue the crust and upper mantle are decoupled based on the viscous deformation of middle and/or lower crust (e.g., Clark & Royden, 2000; Shapiro et al., 2004), while some others argue for vertically coherent deformation of the Tibetan lithosphere (e.g., England & Molnar, 1997; Wang et al., 2008). Our study region, Yunnan, southwest China, is between the eastern Himalaya syntaxis and the mechanically strong Sichuan basin (Figure 7a), which is an ideal place to investigate the mechanisms for eastward expansion and southeastward extrusion of Tibetan Plateau material.

In this study, we used interstation Rayleigh wave phase velocity dispersion data in the period band 5–40 s extracted from vertical-component ambient noise cross-correlation functions (Qiao et al., 2018), which were computed from continuous seismic waveforms in 2008 recorded by 49 permanent stations with about 70-km average station spacing in Yunnan and Guangxi provinces from the China National Seismic Network (Data Management Centre of China National Seismic Network, 2007; Zheng et al., 2010). Figure 7b shows the station distribution and the major geological features in this region.

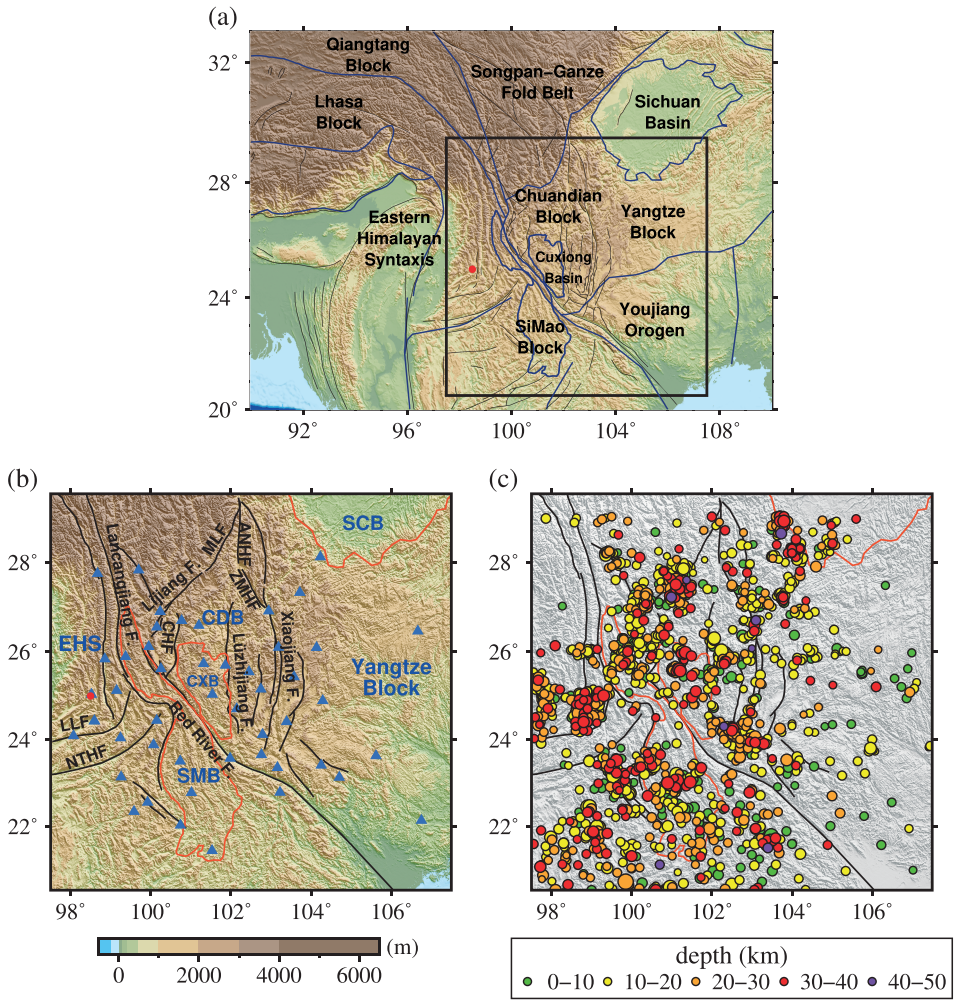

Figure 7. (a) The geological setting of Yunnan, southwest China. (b) Seismic stations and major faults in Yunnan. EHS, eastern Himalayan syntaxis; SCB, Sichuan Basin; CDB, Chuandian Block; CXB, Cuxiong Basin; SMB, Simao Block. Main active faults: ANHF, Anninghe Fault; ZMH, Zhemuhe Fault; CHF, Chenghai Fault; MLF, Muli Fault; LLF, Longling Fault; NTHF, Nantinghe Fault. All of the faults mentioned above are strike-slip faults, except the Lancangjiang Fault. The blue triangles are the seismic stations used in this study. The red dot represents the location of the Tengchong volcano. The red lines are boundaries of the Sichuan Basin, Cuxiong Basin, and Simao Block. (c) The distribution of local earthquakes, with different colors representing different event depths.

The 3-D model of the study region is meshed with a grid spacing of 0.25° × 0.25° horizontally and an interval of 5 km in depth. We choose the isotropic *V*sv model of Shen et al. (2016) as the initial shear wave speed model. Following the workflow of our two-step 3-D joint inversion mentioned in the previous section, the final 3-D isotropic *V*sv and azimuthal anisotropy models are illustrated in Figure 8. The predicted phase velocities and azimuthal anisotropy of the Rayleigh waves are shown in Figure 9. The amplitude of the azimuthal anisotropy is small compared to a previous study by Yao et al. (2010). On the one hand, the amplitude of the results is affected by the regularization parameter λ. In the first-order Tikhonov regularization used in the inversion, the magnitude of azimuthal anisotropy decreases with an increase in λ. On the other hand, the trade-off between anisotropy and heterogeneity still affects the amplitude and the noise in the anisotropic traveltime is also amplified when the recovered isotropic model strongly deviates from the true situation, as we discussed in sections 3.2 and 3.4. We calculate the distribution of the traveltime residuals for the initial model and the results after the first-step isotropic and second-step joint inversion, respectively (Figure 10). It shows an apparent improvement after the two-step inversion, with the standard deviation decreasing from 2.18 to 1.6 s.

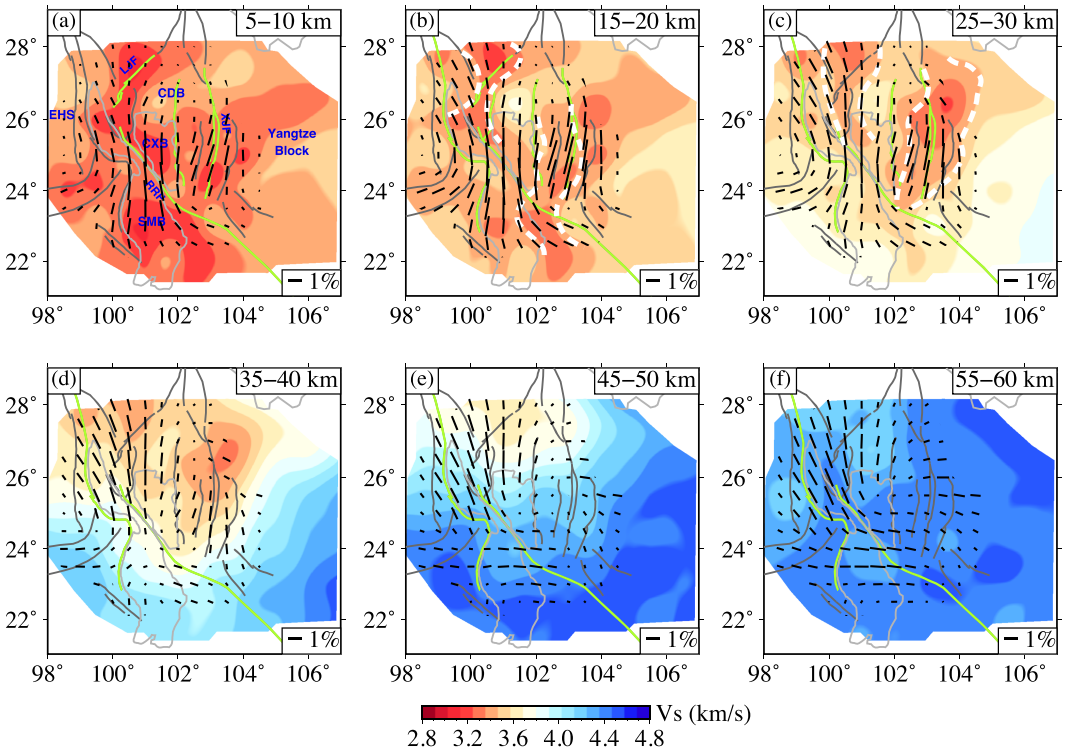

Figure 8. (a–f) Three-dimensional shear wave speed model and corresponding azimuthal anisotropy in the crust and uppermost mantle beneath Yunnan, southwest China. The white dashed lines in (b) and (c) are the approximate boundaries of two channels of low-velocity zones inferred from our model. The background color shows the value of shear wave speed. The short black bars represent the amplitude and fast polarization direction of azimuthal anisotropy. The green lines indicate the local faults mentioned in the main text. Azimuthal anisotropy in eastern Yunnan is not plotted for lack of data coverage.

To check the performance of the inversion results obtained by our algorithm, we conduct conventional checkerboard resolution tests, even though this kind of tests has some drawbacks (Lévěque et al., 1993; Rawlinson & Spakman, 2016). We perform 3-D isotropic (Figure S5) and anisotropic (Figure S6) checkerboard tests with 1° × 1° anomalies, respectively. We generate interstation Rayleigh wave traveltimes with the same source-receiver distribution as in the real case and add 0.5-s Gaussian random noise to the synthetic traveltime data. The results (Figures S7 and S8) suggest that both the isotropic and anisotropic patterns can be retrieved well in most of the regions with proper data constraints. Moreover, another recovery test is conducted to inspect how errors in the isotropic model propagate to the azimuthal anisotropy. We use the isotropic output model of the first-step direct inversion as the "true" model to generate the synthetic data with 0.5-s Gaussian random noise added and then perform inversion following the procedure we mentioned above. As shown in Figure S9, the results can recover the isotropic speed pattern, but the magnitudes of the azimuthal anisotropy are very small, which demonstrates the robustness of the inversion strategy. To assess the uncertainties in the resulting model caused by the noise in the real data, we repeat the inversion strategy using the real data with 0.5-s Gaussian random noise added as estimated from Bensen et al. (2008). The inversion shows similar results in both isotropic and anisotropic velocity structures (Figure S10). The average difference in isotropic *V*s is smaller than 1%, and the average angular deviation of fast axes is less than 6°, which demonstrates the robustness of the inversion strategy and results. In addition, as the isotropic *V*sv reference model of Shen et al. (2016) was developed using Rayleigh wave phase velocities from anisotropic tomography with a denser station array and larger data coverage, the bias from anisotropy was already decoupled. To testify that our model does not depend on the Shen's initial model, we reconduct the two-step 3-D inversion based on a simple *V*sv model (Figure S11) including the influence of Moho depths (He et al., 2014). The obtained result (Figure S12) shows a similar isotropic and anisotropic pattern in most of the inversion region, which also confirms the robustness of our inversion results.

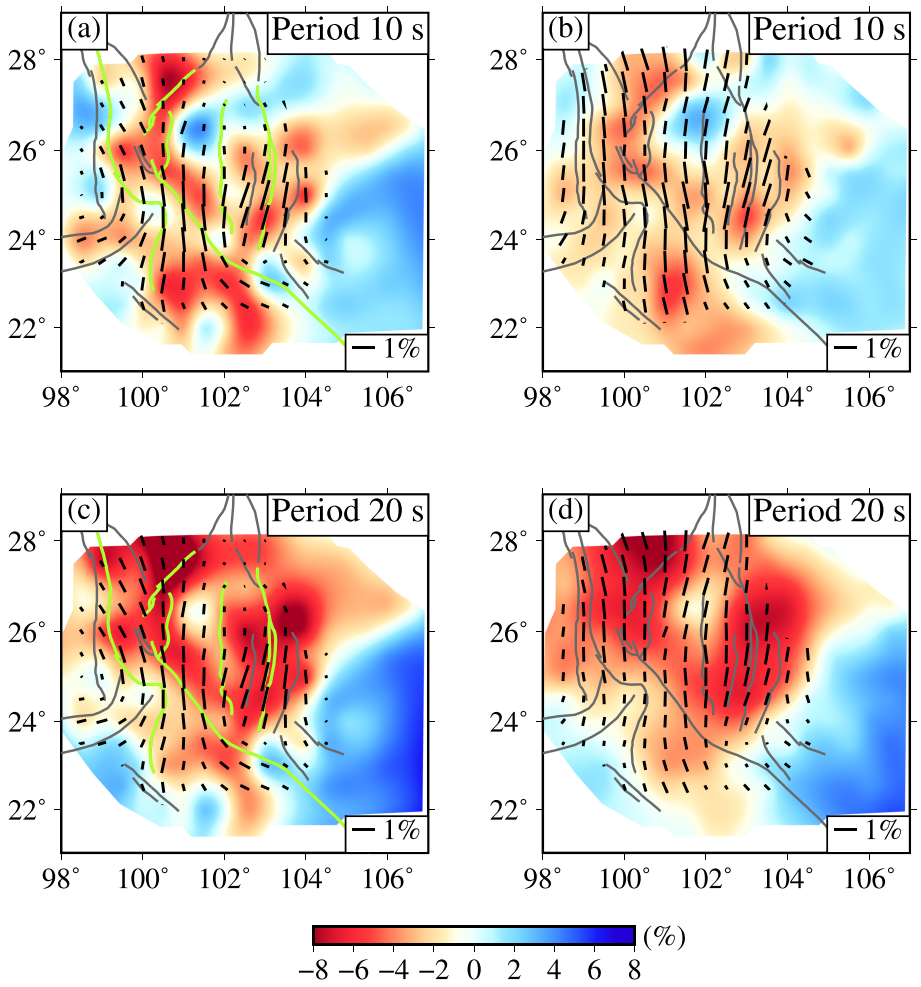

Figure 9. Rayleigh wave phase speed and azimuthal anisotropy (short black bars) maps at T=10 and 20 s (a and c) in Yunnan, southwest China; (b and d) results from ray-based tomography (Shen et al., 2016). The background color represents the phase speed perturbation in percent with respect to the average speed at the corresponding period. The green lines indicate local faults mentioned in the main text at the corresponding period.

We perform a forward calculation of the phase velocities and azimuthal anisotropy for each grid point at different periods (Figures 9a and 9c) based on our inversion results. Compared with the Rayleigh wave phase velocity and azimuthal anisotropy from the linearized ray-based tomography at 10 and 20 s (Figures 9b and 9d; Shen et al., 2016), we find very similar isotropic and anisotropic patterns in the study region, which also supports our model. At a period of 10 s, low phase velocities appear near fault zones, such as the Lijiang Fault, Chenghai Fault, Lancangjiang Fault, Lüzhijiang Fault, Xiaojiang Fault, and Red River Fault. At 20 s, the phase speed pattern changes, with a nearly continuous and prominent low phase speed zone in the Chuandian Block. The fast axes at these periods are almost N-S oriented throughout the Chuandian Block, approximately along the strike directions of nearby faults, such as the Xiaojiang Fault and Lüzhijiang Fault.

The lateral variations in the shear wave speed and the corresponding azimuthal anisotropy at depths of 5–10, 15–20, 25–30, 35–40, 45–50, and 55–60 km are depicted in Figure 8. In general, the isotropic shear wave speeds display complex distributions of low-velocity zones (LVZs) and a coincidence between the boundaries of the LVZs and nearby strike-slip faults. The most active fault in the study region is the left-lateral strike-slip Aninghe-Zemuhe-Xiaojiang fault system, accommodating ~7 mm/year of left slip (Shen et al., 2005). Regional deformation is also notable near the boundary of Songpan-Ganze Fold Belt and southern Chuandian Block by left slip along the Lijiang Fault, and the boundary of SiMao Block by right slip along

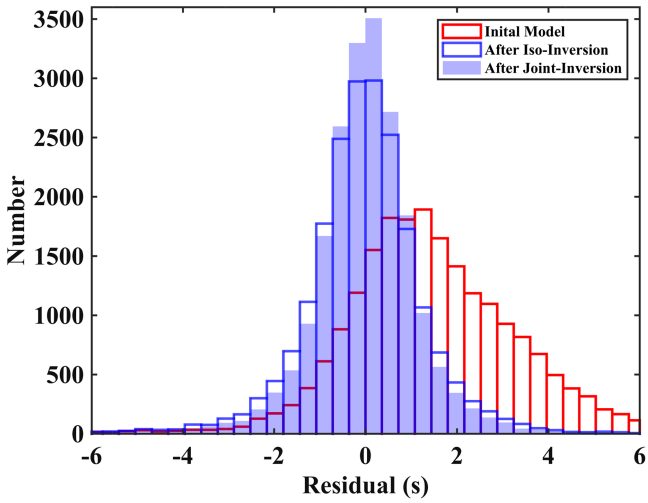

Figure 10. The distribution of Rayleigh wave traveltime residuals for the reference model (red bars) and the results after isotropic inversion (blue bars) and after joint inversion (light blue patches).

the southern segment of Langcangjiang Fault, but appears not to be significant along the Red River Fault currently (Shen et al., 2005).

In the 5- to 10-km depth range, the Simao Block and Cuxiong Basin are characterized by LVZs, which are possibly caused by sedimentary sequences in the upper crust. The areas near the Lijiang Fault, Chenghai Fault, and Xiaojiang Fault also exhibit low-velocity features. In the 15- to 20-km depth range, there are two prominent LVZs that are separated by a relatively high velocity zone between the Chenghai Fault and Lüzhijiang Fault. The western LVZ extends from the northern Chuandian Block southward along the Chenghai Fault and Red River Fault. The eastern LVZ is almost located in the Xiaojiang Fault zone with the Lüzhijiang Fault as its western boundary and crosses the Red River Fault to the south. Both LVZs terminate around the Red River Fault at the 25- to 30- and 35- to 40-km depth range. These two LVZs were also detected by previous tomography studies with similar lateral location and depths (Bao et al., 2015; Chen et al., 2016; Fu et al., 2017; Li et al., 2016; Qiao et al., 2018). In the 45- to 50-km depth range, only one prominent LVZ appears around the Lijiang Fault, in contrast with the surrounding relatively high velocity area, which is mainly controlled by a sharp contrast of Moho depths.

The 3-D direct inversion also reveals substantial variations in the azimuthal anisotropy (Figure 8). In the 5- to 10-km depth range, a striking rotational pattern of fast axes appears around the eastern Himalayan syntaxis, consistent with GPS observations in this region (Zhang et al., 2004). The fast polarization axes at a depth of 5 to 30 km are subparallel to the strike of nearby strike-slip fault systems, that is, NNE-SSW near the Xiaojing Fault, nearly N-S along the Lüzhijiang Fault, and NW-SE near the Red River Fault, which is roughly in accordance with previous azimuthal anisotropy models (Chen et al., 2016; Yao et al., 2010). The patterns of the azimuthal anisotropy from the middle/lower crust to the uppermost mantle change dramatically in the Chuandian Block and Simao Block. In the Simao Block, the fast polarization axes change from the strike of the strike-slip fault in the crust (viz., NNE-SSW near the Lancangjiang Fault and NNW-SSE near the Red River Fault) to a roughly E-W orientation at a depth range of 35–60 km. The fast axes in the northern Chuandian Block remain nearly N-S oriented at deeper depths than the midcrust, while in the southern Chuandian Block the fast axes gradually change to roughly NNW-SSE orientations at a depth range of 55–60 km.

5. Discussion

5.1. The Pros and Cons of the Method

For the traditional two-step anisotropic inversion (e.g., Montagner & Nataf, 1986; Montagner & Tanimoto, 1991; Yao et al., 2010), the isotropic and azimuthally anisotropic phase velocity variations are obtained in the first step of phase velocity tomography using mixed-path dispersion data. Alternatively, the azimuthal anisotropic phase velocity maps can be obtained by eikonal tomography (Lin et al., 2009) or Helmholtz tomography (Lin & Ritzwoller, 2011). In the second step, the pointwise dispersion curve with azimuthal anisotropy can be then inverted for the depth-dependent shear wave speed and its azimuthal anisotropy. In the first step, the inversion of isotropic and azimuthally anisotropic phase velocity parameters may have some trade-off, which is generally weak. In our two-step direct 3-D anisotropic inversion method, we do not need to perform phase velocity tomography but directly take into account the trade-off between the 3-D heterogeneity and anisotropy of shear wave velocities in the second step of joint inversion. If we only invert for the anisotropic parameters in equation (17) while ignoring the isotropic parameters, this trade-off may influence the recovery of azimuthal anisotropy, especially for its amplitude, due to the inaccuracy of the 3-D isotropic model from the first step of the inversion. However, joint inversion for both isotropic shear wave speed perturbation and azimuthal anisotropy (equation (17)) can help to significantly mitigate this trade-off. Also, the first step 3-D tomography of isotropic shear wave speed will provide an excellent starting model for the joint inversion. In general, the change in isotropic wave speed in the second step of the joint

inversion is small. However, it is still important to include isotropic parameters in the joint inversion to mitigate the trade-off between heterogeneity and anisotropy.

Another method to solve this problem is as follows: (1) do the conventional tomography to develop both isotropic and azimuthal anisotropic phase velocities simultaneously, (2) use the isotropic phase velocities from step (1) to generate isotropic traveltimes and then perform 3-D isotropic inversion to get the 3-D *V*sv reference model, and (3) use the anisotropic phase velocities to construct anisotropic traveltimes and then perform 3-D anisotropic inversion.

The trade-off between Moho depth and velocity structure has always been a problem for surface wave inversion. Since we only use Rayleigh wave phase velocity measurements, it is difficult to constrain Moho depth in our 3-D model. Instead, we construct the initial reference model based on previous Moho depth results, for example, from receiver functions as we did in Yunnan, SW China, considering the influence of Moho depth in the tomographic inversion.

The inversion for azimuthal anisotropy depends on good azimuthal coverage of raypaths. In the real data case, the eastern part of the model is abandoned for the lack of data coverage. The raypaths of the phase velocity measurements may vary with periods. For the traditional two-step surface wave tomography (e.g., Yao et al., 2008, 2010), in some extreme cases, when the number of raypaths is small at certain specific periods in some regions, the obtained 2-D phase velocities and corresponding azimuthal anisotropy at some grid points are usually not reliable. Because surface wave tomography at different periods is performed individually, this leads to incorrect inversion of pointwise shear wave speed azimuthal anisotropy. Compared with conventional methods, our proposed 3-D direct inversion for azimuthal anisotropy may make full use of the dispersion measurements at all periods regardless of the number of paths. In addition, the 3-D model regularization used in the tomography can result in an intrinsically smooth 3-D model after inversion. On another hand, the 3-D inversion framework has the advantage of combining other data types, such as body wave traveltimes, to achieve joint 3-D anisotropic inversion.

5.2. The Crustal LVZs in Yunnan, Southwest China

The crustal channel flow model proposed by Royden (1997); Royden et al. (2008) suggests large-scale flow of low viscosity (or mechanically weak) mid–lower crustal material in SE Tibet. Crustal LVZs, typically with weak mechanical properties, sometimes can be used as an indication for channel flow (Bao et al., 2015; Chen et al., 2016; Yao et al., 2008, 2010). Several other geophysical observations also suggest that the LVZs coincide with regions of high heat flow (Hu et al., 2000), high V_P/V_S ratios (Xu et al., 2007), high electrical conductivity (Bai et al., 2010), and unusually high attenuation (Zhao et al., 2013). Two crustal flow channels in SE Tibet have been proposed based on MT and seismic imaging results (Bai et al., 2010; Bao et al., 2015; Qiao et al., 2018).

Our 3-D shear wave speed model depicts the LVZ channel in the Chuandian Block at a depth range of 15–30 km (Figure 8). The western LVZ channel exists around the Lijiang Fault and continues southward along the Chenghai Fault and the western Red River Fault zone, while the eastern LVZ channel extends along the Xiaojiang Fault and connects with the LVZ channel in the central Red River Fault zone. These two LVZ channels are also observed by other tomographic results (Bao et al., 2015; Chen et al., 2016; Qiao et al., 2018). Moreover, a previous azimuthal anisotropy study shows that the fast polarization axes are approximately subparallel to the strikes of LVZ channels (Chen et al., 2016), and our 3-D azimuthal anisotropy model also displays this feature, except for the northern area of the eastern LVZ, which may be affected by the sparse station distribution. Between these two LVZ channels, there exists a high-velocity zone approximately coinciding with the inner zone of the Emeishan large igneous province in the southern Chuandian Block (Qiao et al., 2018), which probably bifurcates the weak mid–lower crustal material in western Sichuan into two channels.

Our 3-D azimuthal anisotropy model shows that the fast polarization axes are subparallel to the local strike-slip faults. The development of some local strike-slip faults, for example, the Lüzhijiang Fault and Xiaojiang Fault, is likely to be related to the LVZs. First, the lateral boundaries of the crustal LVZs approximately coincide with nearby strike-slip faults, for example, the Xiaojiang Fault and Lüzhijiang Fault (Figures 8b and 8c). Moreover, based on the local seismicity (Figure 7c), we find that earthquakes along the local strike-slip faults mainly occur in the depth range of 10–30 km (30–40 km in some places), suggesting the local strike-slip faults are deep rooted and may extend at least to the lower crust. The shearing of the local strike-slip

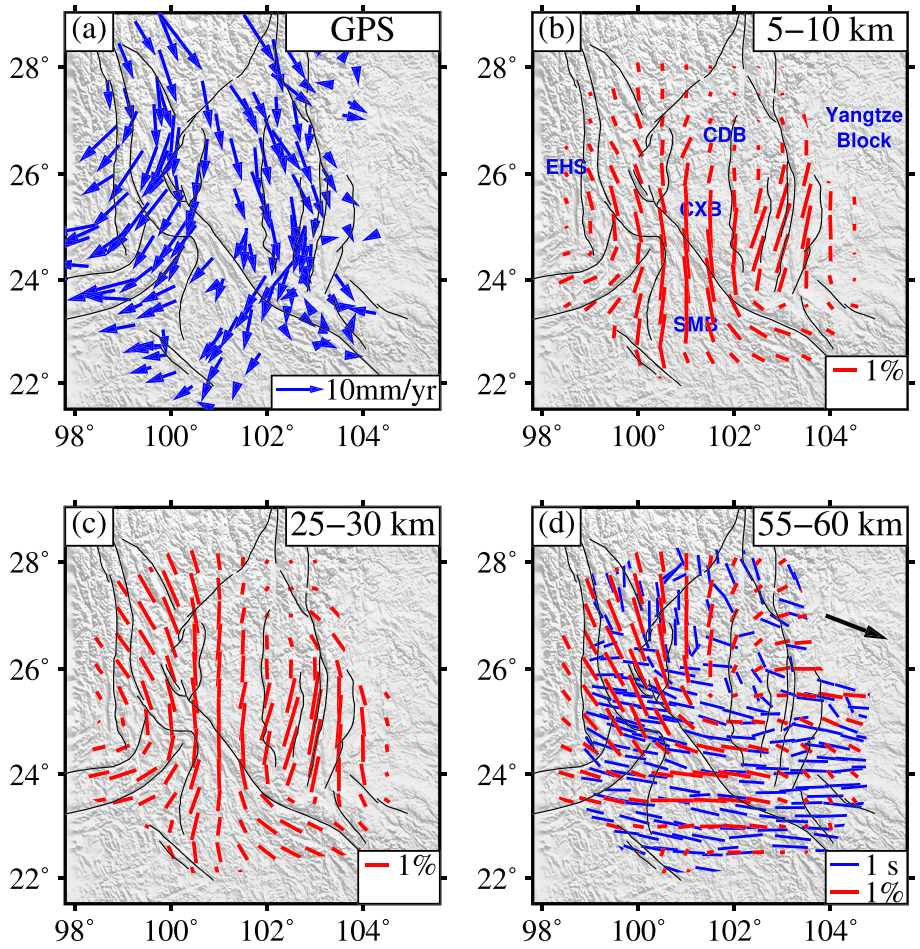

Figure 11. (a) The GPS velocity field with respect to the stable Eurasia plate (blue arrows, data from Zhang et al., 2004). (b, c) The obtained azimuthal anisotropy in this study (red bars) in the depth range of 5–10 and 25–30 km. (d) Comparison of the obtained azimuthal anisotropy (red bars) in the depth range of 55–60 km with teleseismic shear wave splitting measurements (blue bars) of Chang et al. (2015). Black arrows indicate the absolute plate motion of Yunnan in the NNR-MORVEL model (Argus et al., 2011).

faults may in turn affect the fabric of the crustal minerals, that is, the azimuthal anisotropy, in the crust at such depth ranges. Therefore, our results imply a strong and complicated interaction between the LVZs and the local strike-slip faults, which may account for the local strain field in the long term.

5.3. Crust and Mantle Deformation in Yunnan, Southwest China

The patterns of the crust and mantle anisotropy may help us to understand deformation mechanisms in this region. By using a 3-D shear wave speed and azimuthal anisotropy model of the crust and upper mantle in Yunnan, southwest China, as given by Yao et al. (2010) and surface wave data, our model gives the azimuthal anisotropy in the Yunnan area in more detail.

In the uppermost crust, the fast axes of the azimuthal anisotropy are almost parallel to the strike of nearby major faults (e.g., the Xiaojiang Fault, Lüzhijiang Fault, Chenghai Fault, and Nantinghe Fault) and show a curvilinear pattern around the eastern Himalaya syntaxis, similar to that of the GPS velocity field (Figures 11a and 11b). In the Chuandian Block, the azimuthal anisotropy pattern largely resembles the surface motion revealed by GPS, especially areas along the Xiaojiang Fault. In the Simao Block, the fast axes appear subparallel to the strikes of the Langcangjiang Fault and Red River Fault, whereas the pattern in the GPS field is perpendicular to the faults. This difference may be attributed to the fact that the seismic anisotropy reflects structures deformed over their long-term history, while the strain rate field derived from the GPS velocity field represents the instantaneous response to the tectonic forces. From the crust to uppermost

mantle, the fast axes of the azimuthal anisotropy change direction in both the south Chuandian Block and Simao Block, indicating the crust and uppermost mantle have a different deformation pattern (Figure 8). The anisotropic pattern in the study region can be divided into two parts by 26°N due to the apparent Moho depth variation around 26°N (He et al., 2014). To the north, the fast axes keep nearly N-S orientations through the crust (Figures 11b–11d) since the Moho depth in this region is mostly deeper than 55 km (Wang et al., 2017). To the south, in the uppermost mantle (55–60 km), the seismic azimuthal anisotropy shows roughly E-W orientations (Figure 11d), which is parallel to the E-W directions of the absolute plate motion of this area (Argus et al., 2011) and is also consistent with the teleseismic shear wave splitting results (Chang et al., 2015).

Teleseismic shear wave splitting is an important manifestation of anisotropy of the Earth's crust and mantle. Chang et al. (2015) constrained mantle anisotropy with XKS (SKS, SKKS, and PKS) shear wave splitting results in Yunnan and the surrounding area based on the ChinaArray Phase I and permanent stations from Chinese National Seismic Network, which provided much denser measurements in Yunnan and are consistent with previous studies in this area (e.g., Flesch et al., 2005; Wang et al., 2008). As the teleseismic shear wave splitting results in Yunnan are mostly caused by seismic anisotropy in the lithospheric mantle and/or asthenosphere (Chang et al., 2015), we suggest that the anisotropic pattern in our model in the depth range of 55–60 km shows the characteristics of anisotropy of the uppermost mantle in the most of study region to the south of 26°N. In this region, the crustal azimuthal anisotropy is significantly different from the upper mantle anisotropy from both our model and the shear wave splitting results, implying a significant difference in deformation pattern between the crust and upper mantle. Together with the strong mid–lower crustal LVZs (this study; Bao et al., 2015; Qiao et al., 2018) and high crustal Lg attenuation (Zhao et al., 2013), we speculate that large areas of the southern Chuandian Block mostly exhibit decoupled crust and upper mantle deformation, although Wang et al. (2008) suggested that this region is still mechanically coupled from their analysis of GPS data and shear wave splitting measurements. The difference may be due to that the joint analysis of SKS and GPS observations (Wang et al., 2008) is based on the assumption that the crustal anisotropy can be resolved by the strain rate field from GPS observations. However, the strain rate field from GPS data only reflects the present surface deformation and has little insight into the deformation in the deeper crust without other constraints. From our model, we do observe clear depth-varying azimuthal anisotropy in the crust of the study region, which suggests that even within the crust, the upper crust may deform differently from the lower crust. Therefore, we argue that the surface strain rate field derived from GPS data may not represent the deformation pattern (finite strain) of the entire crust in this region.

6. Conclusions

We developed a direct joint inversion method (DAzimSurfTomo) to invert for the 3-D shear wave speed and azimuthal anisotropy using Rayleigh wave dispersion data. This direct inversion method includes two steps: (1) inversion for the 3-D isotropic *V*sv model directly from Rayleigh wave traveltimes (Fang et al., 2015) and (2) iterative joint inversion for both 3-D *V*sv azimuthal anisotropy and additional 3-D isotropic *V*sv perturbation. The joint inversion can significantly mitigate the trade-off between strong heterogeneity and anisotropy. In comparison with the traditional methods, this ray tracing-based approach does not require an intermediate step of construction of 2-D phase velocity azimuthal anisotropy maps. Moreover, it can provide direct lateral constraints on 3-D structures and remedy the drawback of the inaccuracy of the great-circle assumption, especially for complex heterogeneous media. Furthermore, it is computationally efficient compared with adjoint tomography and waveform inversion. The 3-D inversion framework has the advantage of assimilating other data types, such as body wave traveltimes, to jointly constrain the 3-D anisotropic model.

Through a series of synthetic tests, we show the workflow and practicability of our method. Using Rayleigh wave phase velocity dispersion data extracted from the ambient noise interferometry (T = 5–40 s), we successfully apply our method to obtain the crustal shear wave speed and azimuthal anisotropy model in Yunnan. Our 3-D heterogeneity model reveals two crustal LVZs in the depth range of 15–30 km, indicating possible mechanically weak channels for more efficient southward material transport. The depth-dependent azimuthal anisotropy patterns in Yunnan reveal that the fast polarization axes at a depth of 5 to 30 km are consistent with the strike of nearby strike-slip faults, which are also the approximate lateral boundaries of the two LVZs. The local seismicity suggests that the local strike-slip faults are deep rooted and that the shearing of the local strike-slip faults may in turn affect the azimuthal anisotropy in the crust. Therefore, our

model implies a strong and complicated interaction between the LVZs and the local strike-slip faults. In the upper crust, the fast axes of the azimuthal anisotropy are almost parallel to the strike of nearby major faults and show a curvilinear pattern around the eastern Himalayan syntaxis, similar to that of the GPS velocity field. From the upper crust to the uppermost mantle, the azimuthal anisotropy changes its pattern gradually in both the southern Chuandian Block and Simao Block, and the upper crustal azimuthal anisotropy revealed in our study is significantly different from the upper mantle anisotropy from the shear wave splitting results. Together with other geophysical observations, we argue that the southern Chuandian Block mostly exhibits decoupled crust and upper mantle deformation.

Acknowledgments
Waveform data in SW China for this study are provided by the Data Management Centre of China National Seismic Network at the Institute of Geophysics, China Earthquake Administration (doi:10.11998/SeisDmc/SN, http://www.seisdmc.ac.cn). The dispersion data and the model obtained in this study can be found at the GitHub (https://github.com/Chuanming-Liu/Yunnan_Data_Model). Our code can be found at the GitHub (https://github.com/Chuanming-Liu/DAzimSurfTomo). This study is funded by the National Natural Science Foundation of China (Grant 41790464) and the China Earthquake Science Experiment Project, China Earthquake Administration (Project Code 2016CESE0201, 2017CESE0101, and 2018CESE0101). H.-Y. Yang is supported by Chinese Academy Sciences via Grant XDB18010304 and National Natural Science Foundation of China via Grant 41804042. Most figures were plotted using GMT (the Generic Mapping Tools [http://gmt.soest.hawaii.edu]). We are very grateful to the two anonymous reviewers, the Associate Editor, and the Editor, Martha Savage, for their constructive comments upon our original manuscript. We are also grateful to Michael Ritzwoller at the University of Colorado Boulder for his constructive comments.

References

Argus, D., Gordon, R., & DeMets, C. (2011). Geologically current motion of 56 plates relative to the no-net-rotation reference frame. *Geochemistry, Geophysics, Geosystems*, *12*, Q11001. https://doi.org/10.1029/2011gc003751

Aster, R. C., Borchers, B., & Thurber, C. H. (2013). *Parameter estimation and inverse problems*. Academic Press.

Bai, D., Unsworth, M., Meju, M., Ma, X., Teng, J., & Kong, X. (2010). Crustal deformation of the eastern Tibetan Plateau revealed by magnetotelluric imaging. *Nature Geoscience*, *3*(5), 358–362. https://doi.org/10.1038/ngeo830

Bao, X., Sun, X., Xu, M., Eaton, D., Song, X., & Wang, L. (2015). Two crustal low-velocity channels beneath SE Tibet revealed by joint inversion of Rayleigh wave dispersion and receiver functions. *Earth and Planetary Science Letters*, *415*, 16–24. https://doi.org/10.1016/j.epsl.2015.01.020

Barmin, M., Ritzwoller, M., & Levshin, A. (2001). A fast and reliable method for surface wave tomography. *Pure and Applied Geophysics*, *158*(8), 1351–1375. https://doi.org/10.1007/pl00001225

Barruol, G., & Kern, H. (1996). Seismic anisotropy and shear-wave splitting in lower-crustal and upper-mantle rocks from the Ivrea Zone—experimental and calculated data. *Physics of the Earth and Planetary Interiors*, *95*(3-4), 175–194. https://doi.org/10.1016/0031-9201(95)03124-3

Bensen, G. D., Ritzwoller, M. H., Barmin, M. P., Levshin, A. L., Lin, F., Moschetti, M. P., et al. (2007). Processing seismic ambient noise data to obtain reliable broad-band surface wave dispersion measurements. *Geophysical Journal International*, *169*(3), 1239–1260. https://doi.org/10.1111/j.1365-246X.2007.03374.x

Bensen, G. D., Ritzwoller, M. H., & Shapiro, N. M. (2008). Broadband ambient noise surface wave tomography across the United States. *Journal of Geophysical Research*, *113*, B05306. https://doi.org/10.1029/2007JB005248

Brocher, T. (2005). Empirical relations between elastic wavespeeds and density in the Earth's crust. *Bulletin of the Seismological Society of America*, *95*(6), 2081–2092. https://doi.org/10.1785/0120050077

Chang, L., Ding, Z., & Wang, C. (2015). Upper mantle anisotropy beneath the southern segment of North-South tectonic belt. *Chinese Journal of Geophysical*. (in Chinese), *58*(11), 4052–4067.

Chen, H., Zhu, L., & Su, Y. (2016). Low velocity crustal flow and crust–mantle coupling mechanism in Yunnan, SE Tibet, revealed by 3D S-wave velocity and azimuthal anisotropy. *Tectonophysics*, *685*, 8–20. https://doi.org/10.1016/j.tecto.2016.07.007

Clark, M., & Royden, L. (2000). Topographic ooze: Building the eastern margin of Tibet by lower crustal flow. *Geology*, *28*(8), 703. https://doi.org/10.1130/0091-7613(2000)28

Crampin, S., & Chastin, S. (2003). A review of shear wave splitting in the crack-criticalcrust, *Geophysical Journal International*, *155*(1), 221–240.

Dahlen, F., & Tromp, J. (1998). *Theoretical global seismology*. Princeton, NJ: Princeton University Press.

Data Management Centre of China National Seismic Network 2007. Waveform data of China National Seismic Network. Institute of Geophysics, China Earthquake Administration. https://doi.org/10.11998/SeisDmc/SN, http://www.seisdmc.ac.cn.

Debayle, E., Kennett, B., & Priestley, K. (2005). Global azimuthal seismic anisotropy and the unique plate-motion deformation of Australia. *Nature*, *433*(7025), 509–512. https://doi.org/10.1038/nature03247

Ekström, G. (2011). A global model of Love and Rayleigh surface wave dispersion and anisotropy, 25–250 s. *Geophysical Journal International*, *187*(3), 1668–1686. https://doi.org/10.1111/j.1365-246x.2011.05225.x

England, P., & Molnar, P. (1997). Active deformation of Asia: From kinematics to dynamics. *Science*, *278*(5338), 647–650. https://doi.org/10.1126/science.278.5338.647

Fang, H., Yao, H., Zhang, H., Huang, Y., & van der Hilst, R. (2015). Direct inversion of surface wave dispersion for three-dimensional shallow crustal structure based on ray tracing: methodology and application. *Geophysical Journal International*, *201*(3), 1251–1263. https://doi.org/10.1093/gji/ggv080

Flesch, L., Holt, W., Silver, P., Stephenson, M., Wang, C., & Chan, W. (2005). Constraining the extent of crust–mantle coupling in central Asia using GPS, geologic, and shear wave splitting data. *Earth and Planetary Science Letters*, *238*(1-2), 248–268. https://doi.org/10.1016/j.epsl.2005.06.023

Fu, Y., Gao, Y., Li, A., Li, L., & Chen, A. (2017). Lithospheric structure of the southeastern margin of the Tibetan Plateau from Rayleigh wave tomography. *Journal of Geophysical Research: Solid Earth*, *122*, 4631–4644. https://doi.org/10.1002/2016jb013096

Haskell, N. A. (1953). The dispersion of surface waves on multilayered media. *Bulletin of the Seismological Society of America*, *43*(1), 17–34.

He, R., Shang, X., Yu, C., Zhang, H., & Van der Hilst, R. (2014). A unified map of Moho depth and Vp/Vs ratio of continental China by receiver function analysis. *Geophysical Journal International*, *199*(3), 1910–1918. https://doi.org/10.1093/gji/ggu365

Herrmann, R. B. (2013). Computer programs in seismology: An evolving tool for instruction and research. *Seism Research Letters*, *84*(6), 1081–1088. https://doi.org/10.1785/0220110096

Houseman, G., & England, P. (1993). Crustal thickening versus lateral expulsion in the Indian-Asian continental collision. *Journal of Geophysical Research*, *98*(B7), 12,233–12,249. https://doi.org/10.1029/93jb00443

Hu, S., He, L., & Wang, J. (2000). Heat flow in the continental area of China: A new data set. *Earth and Planetary Science Letters*, *179*(2), 407–419. https://doi.org/10.1016/s0012-821x(00)00126-6

Huang, H., Yao, H., & van der Hilst, R. (2010). Radial anisotropy in the crust of SE Tibet and SW China from ambient noise interferometry. *Geophysical Research Letters*, *37*, L21310. https://doi.org/10.1029/2010gl044981

Lévêque, J.-J., Rivera, L., & Wittlinger, G. (1993). On the use of the checker-board test to assess the resolution of tomographic inversions. *Geophysical Journal International*, *115*(1), 313–318. https://doi.org/10.1111/j.1365-246X.1993.tb05605.x

Li, C., Yao, H., Fang, H., Huang, X., Wan, K., Zhang, H., & Wang, K. (2016). 3D near-surface shear-wave velocity structure from ambient-noise tomography and borehole data in the Hefei urban area, China. *Seismological Research Letters*, *87*(4), 882–892. https://doi.org/10.1785/0220150257

Li, M., Zhang, S., Wang, F., Wu, T., & Qin, W. (2016). Crustal and upper-mantle structure of the southeastern Tibetan Plateau from joint analysis of surface wave dispersion and receiver functions. *Journal of Asian Earth Sciences*, *117*, 52–63.

Lin, F., & Ritzwoller, M. (2011). Helmholtz surface wave tomography for isotropic and azimuthally anisotropic structure. *Geophysical Journal International*, *186*(3), 1104–1120. https://doi.org/10.1111/j.1365-246x.2011.05070.x

Lin, F., Ritzwoller, M., & Snieder, R. (2009). Eikonal tomography: Surface wave tomography by phase front tracking across a regional broad-band seismic array. *Geophysical Journal International*, *177*(3), 1091–1110. https://doi.org/10.1111/j.1365-246x.2009.04105.x

Lin, F., Ritzwoller, M., Yang, Y., Moschetti, M., & Fouch, M. (2010). Complex and variable crustal and uppermost mantle seismic anisotropy in the western United States. *Nature Geoscience*, *4*(1), 55–61. https://doi.org/10.1038/ngeo1036

Liu, C., & Yao, H. (2016). Surface wave tomography with spatially varying smoothing based on continuous model regionalization. *Pure and Applied Geophysics*, *174*(3), 937–953. https://doi.org/10.1007/s00024-016-1434-5

Mainprice, D. (2007). Seismic anisotropy of the deep Earth from a mineral and rock physics perspective. *Treatise Geophysical*, *2*, 427–491.

Marone, F., & Romanowicz, B. (2007). The depth distribution of azimuthal anisotropy in the continental upper mantle. *Nature*, *447*(7141), 198–201. https://doi.org/10.1038/nature05742

Molnar, P., & Tapponnier, P. (1975). Cenozoic tectonics of Asia: Effects of a continental collision: Features of recent continental tectonics in Asia can be interpreted as results of the India-Eurasia collision. *Science*, *189*(4201), 419–426. https://doi.org/10.1126/science.189.4201.419

Montagner, J. (1986). 3-dimensional structure of the Indian Ocean inferred from long period surface waves. *Geophysical Research Letters*, *13*(4), 315–318. https://doi.org/10.1029/gl013i004p00315

Montagner, J. (1994). Can seismology tell us anything about convection in the mantle? *Reviews of Geophysics*, *32*(2), 115. https://doi.org/10.1029/94rg00099

Montagner, J., & Jobert, N. (1988). Vectorial tomography—II. Application to the Indian Ocean. *Geophysical Journal International*, *94*(2), 309–344. https://doi.org/10.1111/j.1365-246x.1988.tb05904.x

Montagner, J., & Nataf, H. (1986). A simple method for inverting the azimuthal anisotropy of surface waves. *Journal of Geophysical Research*, *91*(B1), 511. https://doi.org/10.1029/jb091ib01p00511

Montagner, J., & Tanimoto, T. (1991). Global upper mantle tomography of seismic velocities and anisotropies. *Journal of Geophysical Research*, *96*(B12), 20,337–20,351. https://doi.org/10.1029/91jb01890

Moschetti, M., Ritzwoller, M., Lin, F., & Yang, Y. (2010). Seismic evidence for widespread western-US deep-crustal deformation caused by extension. *Nature*, *464*(7290), 885–889. https://doi.org/10.1038/nature08951

Nolet, G. (1990). Partitioned waveform inversion and two-dimensional structure under the network of autonomously recording seismographs. *Journal of Geophysical Research*, *95*(B6), 8499. https://doi.org/10.1029/jb095ib06p08499

Paige, C., & Saunders, M. (1982). LSQR: An algorithm for sparse linear equations and sparse least squares. *ACM Transactions on Mathematical Software*, *8*(1), 43–71. https://doi.org/10.1145/355984.355989

Qiao, L., Yao, H., Lai, Y., Huang, B., & Zhang, P. (2018). Crustal structure of southwest China and northern Vietnam from ambient noise tomography: Implication for the large-scale material transport model in SE Tibet. *Tectonics*, *37*, 1492–1506. https://doi.org/10.1029/2018tc004957

Rawlinson, N., & Sambridge, M. (2004). Wave front evolution in strongly heterogeneous layered media using the fast marching method. *Geophysical Journal International*, *156*(3), 631–647. https://doi.org/10.1111/j.1365-246x.2004.02153.x

Rawlinson, N., & Spakman, W. (2016). On the use of sensitivity tests in seismic tomography. *Geophysical Journal International*, *205*(2), 1221–1243. https://doi.org/10.1093/gji/ggw084

Royden, L. (1997). Surface deformation and lower crustal flow in eastern Tibet. *Science*, *276*(5313), 788–790. https://doi.org/10.1126/science.276.5313.788

Royden, L., Burchfiel, B., & van der Hilst, R. (2008). The geological evolution of the Tibetan Plateau. *Science*, *321*(5892), 1054–1058. https://doi.org/10.1126/science.1155371

Savage, M. (1999). Seismic anisotropy and mantle deformation: What have we learned from shear wave splitting? *Reviews of Geophysics*, *37*(1), 65–106. https://doi.org/10.1029/98rg02075

Shapiro, N., Ritzwoller, M., Molnar, P., & Levin, V. (2004). Thinning and flow of Tibetan crust constrained by seismic anisotropy. *Science*, *305*(5681), 233–236. https://doi.org/10.1126/science.1098276

Shen, W., Ritzwoller, M., Kang, D., Kim, Y., Lin, F., & Ning, J. (2016). A seismic reference model for the crust and uppermost mantle beneath China from surface wave dispersion. *Geophysical Journal International*, *206*(2), 954–979. https://doi.org/10.1093/gji/ggw175

Shen, Z., Lü, J., Wang, M., & Bürgmann, R. (2005). Contemporary crustal deformation around the southeast borderland of the Tibetan Plateau. *Journal of Geophysical Research*, *110*, B11409. https://doi.org/10.1029/2004jb003421

Silveira, G., & Stutzmann, E. (2002). Anisotropic tomography of the Atlantic Ocean. *Physics of the Earth and Planetary Interiors*, *132*(4), 237–248. https://doi.org/10.1016/s0031-9201(02)00076-6

Simons, F., van der Hilst, R., Montagner, J., & Zielhuis, A. (2002). Multimode Rayleigh wave inversion for heterogeneity and azimuthal anisotropy of the Australian upper mantle. *Geophysical Journal International*, *151*(3), 738–754. https://doi.org/10.1046/j.1365-246x.2002.01787.x

Smith, M., & Dahlen, F. (1973). The azimuthal dependence of Love and Rayleigh wave propagation in a slightly anisotropic medium. *Journal of Geophysical Research*, *78*(17), 3321–3333. https://doi.org/10.1029/jb078i017p03321

Tapponnier, P., Peltzer, G., Le Dain, A. Y., Armijo, R., & Cobbold, P. (1982). Propagating extrusion tectonics in Asia: New insights from simple experiments with plasticine. *Geology*, *10*(12), 611–616. https://doi.org/10.1130/0091-7613(1982)10<611:PETIAN>2.0.CO;2

Tapponnier, P., Xu, Z., Roger, F., Meyer, B., Arnaud, N., Wittlinger, G., & Yang, J. (2001). Oblique Stepwise Rise and Growth of the Tibet Plateau. *Science*, *294*(5547), 1671–1677. https://doi.org/10.1126/science.105978

Thomson, W. (1950). Transmission of elastic waves through a stratified solid medium. *Journal of Applied Physics*, *21*(2), 89–93. https://doi.org/10.1063/1.1699629

Wang, C., Flesch, L., Silver, P., Chang, L., & Chan, W. (2008). Evidence for mechanically coupled lithosphere in central Asia and resulting implications. *Geology*, *36*(5), 363. https://doi.org/10.1130/g24450a.1

Wang, W., Wu, J., Fang, L., Lai, G., & Cai, Y. (2017). Crustal thickness and Poisson's ratio in southwest China based on data from dense seismic arrays. *Journal of Geophysical Research: Solid Earth*, *122*, 7219–7235. https://doi.org/10.1002/2017JB013978

Woodhouse, J. H. (1988). The calculation of the eigenfrequencies and eigen function s of the free oscillations of the Earth and the Sun. In D. J. Doornbos (Ed.), *Seismological algorithms*, (pp. 321–370). San Diego, CA: Academic.

Xie, J., Ritzwoller, M., Brownlee, S., & Hacker, B. (2015). Inferring the oriented elastic tensor from surface wave observations: Preliminary application across the western United States. *Geophysical Journal International*, *201*(2), 996–1021. https://doi.org/10.1093/gji/ggv054

Xie, J., Ritzwoller, M., Shen, W., & Wang, W. (2017). Crustal anisotropy across eastern Tibet and surroundings modeled as a depth-dependent tilted hexagonally symmetric medium. *Geophysical Journal International*. https://doi.org/10.1093/gji/ggx004

Xie, J., Ritzwoller, M., Shen, W., Yang, Y., Zheng, Y., & Zhou, L. (2013). Crustal radial anisotropy across Eastern Tibet and the Western Yangtze Craton. *Journal of Geophysical Research: Solid Earth*, *118*, 4226–4252. https://doi.org/10.1002/jgrb.50296

Xu, L., Rondenay, S., & van der Hilst, R. (2007). Structure of the crust beneath the southeastern Tibetan Plateau from teleseismic receiver functions. *Physics of the Earth and Planetary Interiors*, *165*(3-4), 176–193. https://doi.org/10.1016/j.pepi.2007.09.002

Yang, H., & Hung, S. (2005). Validation of ray and wave theoretical travel times in heterogeneous random media. *Geophysical Research Letters*, *32*, L20302. https://doi.org/10.1029/2005gl023501

Yang, H., Zhao, L., & Hung, S. (2010). Synthetic seismograms by normal-mode summation: A new derivation and numerical examples. *Geophysical Journal International*, *183*(3), 1613–1632. https://doi.org/10.1111/j.1365-246x.2010.04820.x

Yang, Y., Ritzwoller, M., Levshin, A., & Shapiro, N. (2007). Ambient noise Rayleigh wave tomography across Europe. *Geophysical Journal International*, *168*(1), 259–274. https://doi.org/10.1111/j.1365-246x.2006.03203.x

Yao, H. (2015). A method for inversion of layered shear wavespeed azimuthal anisotropy from Rayleigh wave dispersion using the neighborhood algorithm. *Earthquake Science*, *28*(1), 59–69. https://doi.org/10.1007/s11589-014-0108-6

Yao, H., Beghein, C., & van der Hilst, R. (2008). Surface wave array tomography in SE Tibet from ambient seismic noise and two-station analysis—II. Crustal and upper-mantle structure. *Geophysical Journal International*, *173*(1), 205–219. https://doi.org/10.1111/j.1365-246x.2007.03696.x

Yao, H., van der Hilst, R., & Montagner, J. (2010). Heterogeneity and anisotropy of the lithosphere of SE Tibet from surface wave array tomography. *Journal of Geophysical Research*, *115*, B12307. https://doi.org/10.1029/2009jb007142

Yao, H. J., van der Hilst, R. D., & de Hoop, M. V. (2006). Surface-wave array tomography in SE Tibet from ambient seismic noise and two-station analysis—I. Phase velocity maps. *Geophysical Journal International*, *166*(2), 732–744. https://doi.org/10.1111/j.1365-246X.2006.03028.x

Yuan, K., & Beghein, C. (2018). A Bayesian method to quantify azimuthal anisotropy model uncertainties: application to global azimuthal anisotropy in the upper mantle and transition zone. *Geophysical Journal International*, *213*(1), 603–622. https://doi.org/10.1093/gji/ggy004

Zhang, P., Shen, Z., Wang, M., Gan, W., Bürgmann, R., & Molnar, P. (2004). Continuous deformation of the Tibetan Plateau from global positioning system data. *Geology*, *32*(9), 809. https://doi.org/10.1130/g20554.1

Zhao, L., Xie, X., He, J., Tian, X., & Yao, Z. (2013). Crustal flow pattern beneath the Tibetan Plateau constrained by regional Lg-wave Q tomography. *Earth and Planetary Science Letters*, *383*, 113–122. https://doi.org/10.1016/j.epsl.2013.09.038

Zheng, X., Yao, Z., Liang, J., & Zheng, J. (2010). The role played and opportunities provided by IGP DMC of China National Seismic Network in Wenchuan Earthquake Disaster Relief and Researches. *Bulletin of the Seismological Society of America*, *100*(5B), 2866–2872. https://doi.org/10.1785/0120090257

Zhu, H., & Tromp, J. (2013). Mapping tectonic deformation in the crust and upper mantle beneath Europe and the North Atlantic Ocean. *Science*, *341*(6148), 871–875. https://doi.org/10.1126/science.1241335